

Modelling hydrologic impacts of light absorbing aerosol deposition on snow at the catchment scale

Felix N. Matt¹, John F. Burkhart^{1,2}, and Joni-Pekka Pietikäinen³

¹Department of Geosciences, University of Oslo, Oslo, Norway

²Statkraft AS, Norway

³Finnish Meteorological Institute, Helsinki, Finland

Correspondence to: Felix N. Matt (f.n.matt@geo.uio.no)

Abstract. Light absorbing impurities in snow and ice (LAISI) originating from atmospheric deposition enhance the snow melt by increasing the absorption of short wave radiation. The consequences are a shortening of the snow duration due to increased snow melt and, at the catchment scale, a temporal shift in the discharge generation during the spring melt season.

In this study, we present a newly developed snow algorithm for application in hydrological models that allows for an additional class of input variables: the deposition mass flux of various species of light absorbing aerosols. To show the sensitivity of different model parameters, we first use the model as 1-D point model forced with representative synthetic data and investigate the impact of parameters and variables specific to the algorithm determining the effect of LAISI. We then demonstrate the significance of the radiative forcing by simulating black carbon deposited on snow of a remote south Norwegian catchment over a six years period, from September 2006 to August 2012. Our simulations suggest a significant impact of BC in snow on the hydrological cycle. Results show an average increase in discharge of 2.5 %, 9.9 %, and 21.4 %, depending on the applied model scenario, over a two months period during the spring melt season compared to simulations where radiative forcing from LAISI is not considered. The increase in discharge is followed by a decrease in discharge due to faster decrease of the catchment's snow covered fraction and a trend to earlier melt in the scenarios where radiative forcing from LAISI is applied. Using a reasonable estimate of critical model parameters, the model simulates realistic BC mixing ratios in surface snow with a strong annual cycle, showing increasing surface BC mixing ratios during spring melt as consequence of melt amplification. However, we further identify large uncertainties in the representation of the surface BC mixing ratio during snow melt and the subsequent consequences for the snowpack evolution.

1 Introduction

The representation of the seasonal snowpack is of outstanding importance in hydrological models aiming for application in cold or mountainous environments. In many mountain regions, the seasonal snowpack contributes a major portion of the water budget, with a contribution of up to 50 % and more to the annual discharge (e.g., Junghans et al., 2011). Snow melt plays a key role in the dynamic of the hydrology of catchments of various high mountain areas such as the Himalayas (Jeelani et al., 2012), the Alps (Junghans et al., 2011) and the Norwegian mountains (Engelhardt et al., 2014), and is an equally important contributor to stream flow generation as rain in these areas. Furthermore, timing and magnitude of the snow melt are major

predictors for flood (Berghuijs et al., 2016) and land slide (Kawagoe et al., 2009) forecasts, and important factors in water resource management and operational hydropower forecasting. Lastly, the extent and the temporal evolution of the snow cover is a controlling factor in the processes determining the growing-season of plants (Jonas et al., 2008). For all these reasons, a good representation of the seasonal snowpack in hydrological models is paramount. However, there are large uncertainties in many variables specifying the temporal evolution of the snowpack, and the snow albedo is one of the most important among those due to the direct effect on the energy input to the snowpack from solar radiation (Anderson, 1976). Fresh snow reflects most of the incoming solar radiation in the near UV and visible spectrum (Warren and Wiscombe, 1980). However, as snow ages and snow grain size increases, the snow albedo will drop as a result of the altered scattering properties of the larger snow grains (Flanner and Zender, 2006). Furthermore, ambient conditions also play a large role. The ratio of diffuse and direct incoming shortwave radiation, the zenith angle of the sun, and the albedo of the underlying ground in combination with the snow thickness can have a large impact on the snow albedo (Warren and Wiscombe, 1980). Of recent significance is the role light absorbing impurities, or particles, which absorb in the range of the solar spectrum, have on albedo when present in the snowpack (further called LAISI, light absorbing impurities in snow and ice) (e.g., Flanner et al., 2007; Painter et al., 2007; Skiles et al., 2012). These LAISI can originate from fossil fuel combustion and forest fires (in the form of black carbon, BC, and organic carbon) (Bond et al., 2013; AMAP, 2015), mineral dust (Painter et al., 2012), volcanic ash (Rhodes et al., 1987), organic compounds in soils (Wang et al., 2013), and biological activity (Lutz et al., 2016), and have species-specific radiative properties.

As LAISI lower the snow albedo, the effect on the snow melt has the potential to alter the hydrological characteristics of catchments where snow melt significantly contributes to the water budget. Recent research investigates the impact of LAISI on discharge generation in mountain regions on different scales. Qian et al. (2011) used a global climate model to simulate the effect black carbon and dust in snow on the hydrological cycle over Tibetan Plateau and found a significant impact on the hydrology, with runoff increasing during late winter/early spring and decreasing during late spring/early summer due to a trend to earlier melt dates. Oaida et al. (2015) showed by implementing radiative transfer calculations to determine snow albedo in the Simple Simplified Biosphere (SSiB) land surface model implementation of the Weather Research and Forecasting (WRF) regional climate model that physically based snow albedo representation can be significantly improved by considering the deposition of light absorbing aerosols in the snowpack evolution. Qian et al. (2009) simulated hydrological impacts due to BC deposition in the western United States using WRF coupled with chemistry (WRF-Chem). They found a decrease in net snow accumulation and spring snowmelt due to BC-in-snow induced increase in surface air temperature.

Only a few studies developed model approaches to resolve the impact of LAISI on the snow melt discharge generation at the catchment scale. Painter et al. (2010) showed that dust, transported from remote places to the Colorado river basin, can have severe implications on the hydrological regime due to disturbances to the discharge generation from snow melt during the spring time, shifting the peak runoff in spring by several weeks and leading to earlier snow free catchments and a decrease in annual runoff. Kaspari et al. (2015) simulated the impact of BC and dust in snow on glacier melt on Mount Olympus, USA, by using measured concentrations in summer horizons and determining the radiative forcing via a radiative transfer model,

indicating enhanced melt during a year of heavy nearby forest fires and coinciding with an increase of observed discharge from the catchment.

Despite these efforts, the direct integration of deposition mass fluxes of light absorbing aerosols in a catchment model is still lacking. To date, there is no rainfall-runoff model with focus on runoff forecast at the catchment scale that is able to consider
5 aerosol deposition mass fluxes alongside snowfall.

On the other hand, there is evidence that including the radiative forcing of LAISI has the potential to further the quality of hydrological predictions: Bryant et al. (2013) showed that during the melt period errors in the operational stream flow prediction of the National Weather Service Colorado Basin River Forecast Center are linearly related to dust radiative forcing in snow and concluded that implementing the effect of LAISI on the snow reflectivity could improve hydrological predictions
10 in regions prone to deposition of light absorbing aerosols on snow, which emphasizes the need for the development of a suitable model approach. Furthermore, we continuously move toward hydrological models with a increasing complex representation of the physical processes involved in the evolution of the seasonal snowpack. Factors that impact the snowpack evolution come into the focus of interest that have been neglected before, such as the impact of LAISI on the snow albedo and subsequent discharge generation in the catchment.

In this study we address this deficiency by introducing a rainfall-runoff model with a newly developed snow algorithm that allows for a new class of model input variables: the deposition mass flux of different species of light absorbing aerosols. The model integrates snowpack dynamics forced by LAISI and allows for analysis at the catchment scale. The algorithm uses a radiative transfer model for snow to account dynamically for the impact of LAISI on the snow albedo and the subsequent impacts on the snow melt and discharge generation. Aside from enabling the user to optionally apply a deposition field, the
20 algorithm depends on standard atmospheric input variables (precipitation, temperature, short wave radiation, wind speed, and relative humidity). To enable a critical evaluation of the newly developed snowpack algorithm, we conduct two independent analyses: i) a 1-D sensitivity study of critical model parameters, and ii) a catchment scale analysis of the impact of LAISI. In both analysis we use BC in snow from wet and dry deposition as a proxy for the impact of LAISI.

We first present an overview over the hydrological model used in this study and the newly developed snow algorithm to treat
25 LAISI in the snowpack in Sect. 2. A description of the catchment used for our study and the input data sets is given in Sect. 3. Sect. 4 describes the 1-D model experiments and the model settings and calibration process in the case study. Lastly our results are presented together with the discussion first for the model experiments, followed by the case study within Sect. 5.

2 Modeling framework and the snowpack algorithm

In the following section we provide descriptions of the hydrologic model (Sect. 2.1) and the formulation of a novel snowpack
30 module used for the analyses (Sect. 2.2).

2.1 Hydrologic Model Framework

For the analysis, we use Statkraft's hydrologic forecasting toolbox (Shyft; <https://github.com/statkraft/shyft>), a model framework developed for hydropower forecasting. The concept of Shyft follows the idea that a hydrological model can be expressed as a sequence of well known routines, each describing a certain aspect of the represented hydrological processes. Which processes are represented depend on the purpose of the model and the requirements of the user. The sequence of routines, the so called "methods-stack", is then run on a cell by cell basis, where the cell loosely represents an area of similar time-invariant geographical data (e.g. topographic properties or land type) with no specific restriction to cell geometry or area. The Shyft framework allows for the paradigm of distributed, conceptual parameter models, and more physically based approaches. Standard model input variables are temperature, precipitation, wind speed, relative humidity and shortwave radiation. The methods-stack used herein consists of (i) a single-equation implementation to determine the potential evapotranspiration, (ii) a newly developed snowpack algorithm using an online radiative transfer solution for snow to account for the effect of LAISI on the snow albedo, and (iii) a first order nonlinear differential equation to calculate the catchment response to precipitation, snow melt and evapotranspiration. (i) and (iii) are described in more detail herein, while (ii) is described in detail in Sect. 2.2.

To determine the potential evapotranspiration, E_{pot} , we use the method according to Priestley and Taylor (1972)

$$E_{pot} = \frac{a}{\lambda} \cdot \frac{s(T_a)}{s(T_a) + \gamma} \cdot R_n \quad (1)$$

with $a = 1.26$ being a dimensionless empirical multiplier, γ the psychrometric constant, $s(T_a)$ the slope of the relationship between the saturation vapour pressure and the temperature T_a , λ the latent heat of vaporization and R_n the net radiation.

The catchment response to precipitation and snow melt is determined using the approach of Kirchner (2009), who describes catchment discharge from a simple first order nonlinear differential equation. Following Kirchner's suggestion, we solve the log transformed formulation

$$\frac{d(\ln(Q))}{dt} = g(Q) \left(\frac{P - E}{Q} - 1 \right) \quad (2)$$

due to numerical instabilities of the original formulation. In Eq. (2), Q is the catchment discharge, E the evapotranspiration, and P the precipitation.

We assume that the sensitivity function, $g(Q)$, has the same form as described in Kirchner (2009):

$$\ln(g(Q)) \approx c_1 + c_2 \ln(Q) + c_3 (\ln(Q))^2 \quad (3)$$

with c_1 , c_2 and c_3 being the only catchment specific parameters, which we estimate by standard model calibration of simulated discharge against observed discharge. In contrast to Kirchner (2009)'s approach, we use the liquid water outflow from the snow routine instead of precipitation P in Eq. (2) (Kirchner (2009) used snow-free catchments in his analysis). The outflow from the snow routine can be liquid precipitation, melt water, or a combination of both.

2.2 A new snowpack module for LAISI

To account for snow in the model, we developed a snow-algorithm to solve the energy balance

$$\frac{\delta F}{\delta t} = K_{in}(1 - \alpha) + L_{in} + L_{out} + H_s + H_l + R \quad (4)$$

with the incoming shortwave radiation flux K_{in} , the incoming and outgoing longwave radiation fluxes L_{in} and L_{out} , the
5 sensible and latent heat fluxes H_s and H_l , and the heat contribution from rain R (fluxes are considered to be positive when
directed into the snowpack and as such an energy source to the snowpack). $\frac{\delta F}{\delta t}$ is the net energy flux into (or out of) the
snowpack (fluxes are considered to be positive when directed into the snowpack).

L_{in} and L_{out} are calculated using the Stephan-Boltzmann law, with L_{in} depending on the air temperature T_a and L_{out} on
the snow surface temperature T_{ss} , calculated as $T_{ss} = 1.16 \cdot T_a - 2.09$ (Hegdahl et al., 2016). The latent and sensible heat fluxes
10 are calculated using a bulk-transfer approach that depends on wind speed, temperature and relative humidity (Hegdahl et al.,
2016).

The main addition provided in the algorithm described herein is the implementation of a radiative transfer solution for
the dynamical calculation of snow albedo, α . The implementation allows a new class of model input variables, wet and dry
deposition rates of light absorbing aerosols. From this, the model is able to simulate the impact of dust, black carbon, volcanic
15 ash or other aerosol deposition on snow albedo, snow melt and runoff. To account for the mass balance of LAISI in the
snowpack while maintaining a representation of sub-grid snow variability and snow cover fraction (SCF), the energy balance
based snow algorithm underlies a tiling approach, where a grid-cell's snowfall is apportioned to sub-grid units following a
gamma distribution.

In the following we present: (i) an introduction to the radiative transfer calculations required to represent LAISI in the
20 snowpack (Sect. 2.2.1), and (ii) the sub-gridscale tiling approach to represent snowpack spatial variability (Sect. 2.2.2).

2.2.1 Aerosols in the snowpack

Wiscombe and Warren (1980) and Warren and Wiscombe (1980) developed a robust and elegant model for snow albedo that
remains today as a standard. Critical to their approach was the ability to account for: (i) wide variability in ice absorption
with wavelength, (ii) the forward scattering of snow grains, and (iii) both diffuse and direct beam radiation at the surface.
25 Furthermore, and of particular importance to the success of the approach, the model relies on observable parameters.

Both the albedo of clean snow and the effect of LAISI on the snow albedo strongly depend on the snow grain effective radius
(or optical grain size) r (Warren and Wiscombe, 1980), which alters as snow ages. r can be related to the specific surface area
(SSA), representing the ratio of surface area per unit mass of the snow grain (Roy et al., 2013),

$$r = \frac{3}{\rho_{ice} \cdot SSA} \quad (5)$$

30 with ρ_{ice} the density of ice.

In our model, we compute the evolution of SSA in dry snow following Taillandier et al. (2007) as

$$SSA(t) = [0.629 \cdot SSA_0 - 15.0 \cdot (T_s - 11.2)] - [0.076 \cdot SSA_0 - 1.76 \cdot (T_s - 2.96)] \ln \left\{ t + \exp \left(\frac{-0.371 \cdot SSA_0 - 15.0 \cdot (T_s - 11.2)}{0.076 \cdot SSA_0 - 1.76 \cdot (T_s - 2.96)} \right) \right\}, \quad (6)$$

5 where t is the age of the snow layer (hours), SSA_0 is the SSA at $t=0$ ($\text{cm}^2 \text{ g}^{-1}$), and T_s is the snow temperature ($^{\circ}\text{C}$). The evolution of SSA in wet snow is calculated according to Eq. 5 and Brun (1989) as

$$\Delta r = \frac{C_1 + C_2 \cdot \Theta^3}{r^2 \cdot 4\pi}, \quad (7)$$

where $C_1=1.1 \cdot 10^{-3} \text{ mm}^3 \text{ d}^{-1}$ and $C_2 = 3.7 \cdot 10^{-5} \text{ mm}^3 \text{ d}^{-1}$ are empirical coefficients. Θ is the liquid water content of snow in mass percentage. SSA_0 is set to $73.0 \text{ m}^2 \text{ kg}^{-1}$ (Domine et al., 2007) and we set the minimum snowfall required to reset the
10 SAA to 5 mm snow water equivalent (SWE).

To solve for the effect of light absorption of LAISI in the snowpack on the snow albedo, we have integrated a two-layer adaption of the Snow, Ice, and Aerosol Radiative (SNICAR) model (Flanner et al., 2007, 2009) into the energy and mass budget calculations. By providing the solar zenith angle of the sun, the optical grain size r of snow, mixing ratios of LAISI in the snow layers and SWE of each layer, SNICAR calculates the snow albedo for a number of spectral bands. To achieve
15 this, SNICAR utilizes the theory from Wiscombe and Warren (1980) and the two-stream, multilayer radiative approximation of Toon et al. (1989). Following Flanner et al. (2007), our implementation of SNICAR uses five spectral bands (0.3-0.7, 0.7-1.0, 1.0-1.2, 1.2-1.5, and 1.5-5.0 μm) in order to maintain computational efficiency. Flanner et al. (2007) compared results from 5 bands scheme to the default 470 bands scheme in SNICAR and concluded that relative errors are less than 0.5%. The incident flux were simulated offline assuming mid-latitude winter clear- and cloudy-sky conditions.

20 The absorbing effect of LAISI is most efficient when the LAISI reside at or close to the snow surface (Warren and Wiscombe, 1980). As snow melts LAISI can remain near the surface due to inefficient melt scavenging, which leads to an increase in the near surface concentration of LAISI and thus a further decrease in the snow albedo; the so called melt amplification (e.g., Xu et al., 2012; Doherty et al., 2013; Sterle et al., 2013; Doherty et al., 2016). Field observations suggest that the magnitude of this effect is determined by the particle size and the hydrophobicity of the respective LAISI (Doherty et al., 2013). Conway
25 et al. (1996) observed vertical redistribution and the effect on the snow albedo by adding volcanic ash and hydrophilic and hydrophobic BC to the snow surface of a natural snowpack. Flanner et al. (2007) used the results from Conway et al. to determine the scavenging ratios, specifying the ratio of BC contained in the melting snow that is flushed out with the melt water, of both hydrophilic and hydrophobic BC. They found the scavenging ratio for hydrophobic BC, k_{phob} , to be 0.03, and for hydrophilic BC, k_{phil} , 0.2. Doherty et al. (2013) found similar results by observing BC mixing ratios close to the surface
30 of melting snow. Recent studies report efficient removal of BC with melt water (Lazarcik et al., 2017), revealing large gaps in the understanding of the process.

To represent the evolution of LAISI mixing ratio near the snow surface, we treat LAISI in two layers in our model: (i) a surface layer with a time invariant maximum depth (in mm SWE), where the concentration of each LAISI species is calculated

from a uniform mixing of the layer's snow with either falling snow with a certain mixing ratio of aerosol (wet deposition) or aerosol from atmospheric dry deposition; and (ii) a bottom layer, representing the snow exceeding the maximum depth of the surface layer. Following Krinner et al. (2006), we apply a maximum surface layer thickness of 8 mm. Krinner et al. (2006) suggests this value based on observations of 1 cm thick dirty layers in alpine firn cores used to identify summer horizons. Due to potential accumulation of LAISI in surface snow via dry deposition and melt amplification, we expect the simulated surface mixing ratios of LAISI to be sensitive to the surface layer thickness of our model. For this reason, we use a factor of 2 to the maximal surface layer thickness to account for the uncertainty.

To allow for melt amplification in the model, we include LAISI mass fluxes between the two layers during snow accumulation and snow melt. Generalizing Jacobson (2004)'s representation of LAISI mass loss due to meltwater scavenging for multiple snow layers (Flanner et al., 2007), we characterize the magnitude of melt scavenging using the scavenging ratio k and calculate the temporal change of BC mass m_s in the surface layer as

$$\frac{dm_s}{dt} = -kq_s c_s + D, \quad (8)$$

and the change of BC mass m_b in the bottom layer as

$$\frac{dm_b}{dt} = k(q_s c_s - q_b c_b). \quad (9)$$

Herein, q_s and q_b are the mass fluxes of melt water from the surface to the bottom layer and out of the bottom layer, respectively, and c_s and c_b are the mass mixing ratios of BC in the respective layer. D is the atmospheric deposition mass flux. A value for k of <1 is equal to a scavenging efficiency of less than 100% and hence allows for accumulation of LAISI in the surface layer during melt. In our analysis, we account for hydrophobic and hydrophilic BC by distinguishing between the type of deposition mechanism (hydrophilic BC predominantly from wet deposition, hydrophobic BC for dry deposition). By following Flanner et al. (2007), we set k_{phob} to 0.03 and k_{phil} to 0.2, and account for the large uncertainty by using an order of magnitude variation on k_{phob} and k_{phil} . Like Flanner et al. (2007), we treat aged, hydrophilic BC as sulphate coated to account for the net increase in the mass absorption cross section (MAC) by 1.5 at $\lambda=550$ nm compared to hydrophobic BC caused by the ageing of BC (reducing effect on MAC) and particle coating from condensation of weakly absorbing compounds (enhancing effect on MAC) suggested by Bond et al. (2006). As a consequence, hydrophilic BC absorbs stronger than hydrophobic BC under the same conditions. On the other hand, hydrophilic BC undergoes a more efficient melt scavenging. The competing mechanisms are subjects of the 1-D sensitivity study in Sect. 5.1.3.

2.2.2 Sub-grid variability in snow depth and snow cover

The representation of sub-grid snow variability can play a key role in modelling the hydrology of areas with a seasonal snowpack (e.g., Hartmann et al., 1999). Several approaches exist to capture the sub-grid snow covered fraction (SCF) and distribution of SWE. Statistical approaches often use so called snow depletion curves to describe a relationship between a prognostic snow

variable (e.g SWE, accumulated melt depth) and regional observations of SCF, (e.g., Liston, 2004; Luce and Tarboton, 2004; Kolberg and Gottschalk, 2010). However, such approaches do not allow for explicit treatment of snow layers, which is required when simulating the mixing ratios of LAISI. In our model, we follow (Aas et al., 2017) by assuming that the sub-grid spatial distribution of each single event of solid precipitation follows a certain probability distribution function. From this distribution we calculate multiplication factors, which then are used to assign the snowfall of a model grid cell to a number of sub-grid computational elements, the so called tiles (Aas et al., 2017). The snow algorithm described herein is executed for each of the tiles separately. This implies that variables related to the snow state, such as SWE, liquid water content, impurity content, and snow albedo differ among the tiles. This also allows to simulate the sub-grid variability in impurity content. To calculate the multiplication factors, we assume that the sub-grid redistributed snow follows a gamma distribution (see e.g., Kolberg and Gottschalk, 2010; Gislås et al., 2016), determined by the coefficient of variation (CV). CV values were derived based on work done by Gislås et al. (2016), who used Winstral and Marks (2002)'s terrain-based parametrization to model snow redistribution in Norway by accounting for wind effects during the snow accumulation period over a digital elevation model with 10 m resolution. Gislås et al. (2016) calibrated the redistribution model with snow depth data from Airborne Laser Scanning (ALS) over the Hardangervidda mountain plateau (see Melvold and Skaugen (2013)) and evaluated with snow depth data from ground penetrating radar observations at Finse, both located in Southern Norway. The detailed scheme is described in Gislås et al. (2016). In the case study presented in Sect. 5.2, we use the CV values from Gislås et al. (2016) to derive a linear relationship between the model cell's elevation and the corresponding CV value by simple linear regression (see Fig. 1a), which results in a R^2 -value of 0.71 and a p-value of smaller than $2.0e-5$ for the study area. The linear relationship is only applied to cells with an areal forest cover fraction of lower than or equal to 0.5. For cells with a forest cover fraction of higher than 0.5, a constant snow CV value of 0.17 is used, following the findings of Liston (2004) for high latitude, mountainous forest. Examples of multiplication factors for forested cells and forest free cells for a different CV values are shown in Fig. 1b.

3 Site description, meteorologic model input and atmospheric deposition data

We selected the unregulated upper Atna catchment for our analysis. This catchment is located in a high elevation region of southern Norway (left Fig. 2). The watershed covers an area of 463 km^2 and ranges in elevation from 700 masl at the outlet at lake Atnsjoen to over 2000 masl in the Rondane mountains in the western part of the watershed (right Fig. 2), with approximately 90 % of the area above the forest limit. The average annual precipitation in the watershed during the study period is approximately 655 mm, where most precipitation falls as rain in summer. The mean annual discharge is approximately $11 \text{ m}^3\text{s}^{-1}$, with low flows of $1\text{-}3 \text{ m}^3\text{s}^{-1}$ during the winter months and peak flows of over $130 \text{ m}^3\text{s}^{-1}$ during the spring melt season.

For the meteorological model input of precipitation, temperature, relative humidity and wind speed we use daily observations from the Norwegian Water Resources and Energy Directorate (NVE) and the Norwegian Meteorological Institute (MET). Four meteorological stations are located in the watershed at elevations between 701 and 780 masl along the Atna river, two of these measuring precipitation and two measuring temperature (see right Fig. 2). Observations of relative humidity and

wind speed originate from two stations at locations close by the catchment (not shown in right Fig. 2). Further information about the stations are given in Table 1. Due to poor availability of continuous solar radiation observations in Norway, we use gridded global radiation data from the Water and Global Change (WATCH) Forcing Data methodology applied to ERA-Interim reanalysis data (WFDEI; Weedon et al. (2014)) with a resolution of 0.5° . We use BC aerosol deposition rates as proxy for LAISI sources. Further LAISI such as mineral dust are not considered which might lead to errors (discussed in Sect. 5.3). The BC deposition mass fluxes are simulated with the regional aerosol-climate model REMO-HAM (described in more detail in Sect. 3.1). Discharge observations are from a station located at the outlet of the catchment at lake Atnsjoen and are used for model calibration and validation. For the 1-D sensitivity study of Sect. 5.1 we developed representative model input based on the meteorological conditions in this catchment.

10 3.1 Atmospheric deposition of black carbon from the REMO-HAM model

The wet and dry deposition rates of BC for the study area are generated using the regional aerosol-climate model REMO-HAM (Pietikäinen et al., 2012). The core of the model is a hydrostatic, three-dimensional atmosphere model developed at the Max Planck Institute for Meteorology in Hamburg. With the aerosol configuration, the model incorporates the HAM (Hamburg Aerosol Module) by Stier et al. (2005) and Zhang et al. (2012). HAM calculates the aerosols distributions using 7 log-normal modes and includes all the main aerosol processes.

For the simulations, we follow the approach of Hienola et al. (2013), but with changes to the emission inventory: Hienola et al. (2013) used emissions based on the AeroCom emission inventory for the year 2000 (see Dentener et al., 2006). In the REMO-HAM simulations conducted herein, emissions are made by the International Institute for Applied Systems Analysis (IIASA) and are based on the Evaluating the Climate and Air Quality Impacts of Short-Lived Pollutants (ECLIPSE) V5a inventory for the years 2005, 2010, and 2015 (years in between were linearly interpolated) (Klimont et al., 2016b, a). We updated also other emissions modules (wildfire, aviation, and shipping) following the approaches presented in Pietikäinen et al. (2015). The only difference to Pietikäinen et al. (2015) in this work is that we used the Global Fire Emissions Database (GFED) version 4 based on an updated version of van der Werf et al. (2010).

REMO-HAM was used for the same European domain as in Pietikäinen et al. (2012) using 0.44° spatial resolution (50 km), 27 vertical levels and 3 minutes time step. The ERA-Interim re-analysis data was utilized at the lateral boundaries for meteorological forcing (Dee et al., 2011) and for the lateral aerosol forcing, data from the global aerosol-climate model ECHAM-HAMMOZ (version echam6.1.0-ham2.2) was used. ECHAM-HAMMOZ was simulated in a nudging mode, i.e. the model's meteorology was forced to follow ERA-Interim data, and the ECLIPSE emissions were used (plus other updated emission modules shown in Pietikäinen et al. (2015)). The boundaries of REMO-HAM were updated every 6 hours for both meteorological and aerosol related variables. Simulations with REMO-HAM were conducted for the time period of 01.07.2004 - 31.08.2012 and the time period used in the analysis herein is from 01.09.2006 onwards. The initial state for the model was taken from the boundary data, except for the soil parameters which were taken from a previous long-term simulation for the same domain (a so called warm-start). The output frequency of REMO-HAM was 3 hours and the total BC deposition flux was calculated from the accumulated dry and wet deposition and sedimentation fluxes.

In the snow algorithm used in this study, dry deposition and sedimentation are treated the same way. Herein, dry deposition refers to the sum of REMO-HAM dry deposition and sedimentation.

4 Model experiments and calibration

Our analysis is in two parts in Sect. 5. First we present a 1-D sensitivity study investigating the impact of parameters and variables specific to the algorithm determining the effect of LAISI (Sect. 5.1). We then demonstrate the significance of BC in snow radiative forcing on the catchment scale in a case study by simulating the impact of wet and dry deposition of BC in a remote south Norwegian catchment (Sect. 5.2).

We assume uncertainties of the LAISI radiative forcing to originate mainly from the model representation of surface layer thickness, melt scavenging of BC, and uncertainties in the deposition input data. To account for the uncertainties, we declare minimum (min), central (mid), and maximum (max) effect estimates to each of the critical parameters, outlined together with further model parameters in Table 2. The min, mid, and max estimates are both subjects of analysis in the sensitivity study (further described in Sect. 4.1) and used in the case study to give an uncertainty estimate of the LAISI effect on the hydrologic variables (further described in Sect. 4.2). We investigate the impact of BC impurities on the response variables by comparing the results from Aerosol Radiative Forcing model experiments ("ARF" scenarios) to simulations in which all BC deposition rates are set to zero ("no-ARF" scenario).

4.1 1-D sensitivity study experiments

For the 1-D sensitivity study presented in Sect. 5.1, we use synthetic input data to study the evolution of snowpacks under constant melting conditions in order to identify the impact of different model settings: the impact of (i) the maximum surface layer thickness, (ii) the scavenging ratio sole, and (iii) the impact of the scavenging ratio with respect to the BC species. Furthermore, we investigate how LAISI impact snowpacks of different depths, but same LAISI mixing ratio at melt onset. We run the model with model parameters as outlined in Table 2 if not otherwise specified.

The model input applied for melting is based on the average meteorological conditions during the melt season from mid March until mid July of the Atnsjoen catchment. In our sensitivity experiments, all snowpacks have 250 mm SWE of snow with a mixing ratio of 35 ng g^{-1} in both surface and bottom layer at melt onset. These values are representative of the upper 50% of tiles at winter snow maximum in the Atnsjoen catchment during the study period of the case study. During the melt period, we exclude fresh snowfall and dry deposition, in order to isolate the effect of the tested model parameters on the snowpack evolution under melt conditions. This might lead to an underestimation of total BC mass in the snow column.

4.2 Case study model setup and calibration

We investigate the impact of BC aerosol deposition on the catchment hydrology of a Norwegian catchment over a study period of 6 years, from September 2006 to September 2012. The station based input data described above is interpolated to the simulation cells ($1 \times 1 \text{ km}^2$ and accordingly smaller cells at the catchment borders; right Fig. 2) using Shyft's interpolation

algorithms. For temperature Bayesian Kriging (Diggle and Ribeiro, 2007) is used. For precipitation, BC deposition rates, wind speed, and relative humidity interpolation to the model cells is via inverse distance weighting. A 5% increase in precipitation for every 100 m increase in altitude (Førland, 1979) is used for the precipitation interpolation.

To calibrate the model against observed discharge, we first run a split-sample calibration (Klemes, 1986) using the first 3 years (1 September 2006 to 31 October 2009) of the study period as calibration period and the following 3 years (1 September 2009 to 31 October 2012) for model validation. For parameter estimation, we use the BOBYQA algorithm for bound constrained optimization (Powell, 2009). To assess the predictive efficiency of the model we use the Nash-Sutcliffe model efficiency (NSE).

$$NSE = 1 - \frac{\sum_{t=0}^T (Q_o^t - Q_s^t)^2}{\sum_{t=0}^T (Q_o^t - \overline{Q_o})^2} \quad (10)$$

where Q_o^t and Q_s^t are the observed and simulated discharge at time t , respectively, and $\overline{Q_o}$ is the mean observed discharge over the assessed period. Model calibration is run with mid-estimates for all model parameters impacting the handling and effect of LAISI in the snowpack and aerosol depositions as simulated from REMO-HAM during model calibration. Those parameters and further model parameters, including the parameters estimated during calibration, are listed in the left column of Table 2. We investigate the uncertainty in the effect of LAISI on snow melt by using the min and max effect parameter estimates from Table 2, while holding constant all other model parameters as estimated during calibration. To assess the gross effect of LAISI we compare the simulations to equivalent simulations in which ARF is not included.

5 Results and Discussion

In the following, we first present in Sect. 5.1 the role of model parameters and variables critical to the effect of LAISI on the development of a melting snowpack by using our new snow algorithm as a point model. We then present the results of the case study in Sect. 5.2, where we examine the significance of the LAISI radiative forcing for hydrological processes by simulating the impact of BC deposition on the snow melt and discharge generation in a snow dominated mountain catchment (Sect. 5.2).

5.1 1-D sensitivity studies

5.1.1 Sensitivity to surface layer thickness

To investigate the impact of the maximum surface layer thickness of the model, we run simulations with synthetic forcing and use maximal surface layer thicknesses of 4.0 mm SWE (max estimate, see Tabel 2), 8.0 mm SWE (mid estimate), 16.0 mm SWE (min estimate). Additionally we include a single layer model with a vertically uniform distribution of BC in the analysis and for comparison a simulation with clean snow. Fig. 3a shows the effect of the different maximum surface layer thicknesses on the melting snowpack, with mid-estimates for further model parameters according to Table 2. The maximum surface layer thickness strongly determines the surface BC mixing ratio over the melt season. During snow melt, surface BC

increases up to a factor of circa 10, 20 and about 30 for maximum surface layer thicknesses of 16.0 mm SWE, 8.0 mm SWE, and 4.0 mm SWE, compared to the pre-melt season BC mixing ratio (35 ng g^{-1}). Since the model input used in the sensitivity study during the melt period does exclude fresh snowfall and dry deposition, the increase in surface BC mixing ratio is due to melt amplification solely. The importance of BC accumulation in surface snow is discussed controversially in the literature.

5 While several studies report a significant increase in surface BC mixing ratio during melt (Doherty et al., 2013; Sterle et al., 2013) of up to an order of magnitude (Sterle et al., 2013) and more (Xu et al., 2012), others report highly efficient scavenging with melt (Lazarcik et al., 2017). Over most of the melt period, our results show a factor increase between 5 and 15. Only at the end of the melt season, higher factor increases are reached. To this point of time, however, the snowpack is typically very thin and effects on discharge generation due to very high increase in surface BC should be small.

10 For the three 2-layer scenarios (green, purple and red curves in Fig. 3a), the resulting difference on the albedo and melt rate are small, even though the increase in surface layer mixing ratio during the melt season differs strongly among the scenarios. The relatively small differences in snowpack evolution among the two-layer models, despite the large differences in surface BC, result from the fact that for all two-layer models the surface layer thickness is much thinner than the penetration depth of shortwave radiation. For example, in clean snow with an optical grain size of 50 μm , the radiative intensity diminishes to

15 $\frac{1}{e}$ of its surface value (the so called penetration depth) in 25.5 mm SWE. For snow with an optical grain size of 1000 μm , the penetration depth increases to 117 mm SWE (both results from Flanner et al., 2007, assuming a wavelength of 550 nm and a solar zenith angle of 60°). Thus, BC in the surface layer absorb efficiently in all 2-layer scenarios and the difference in the albedo is relatively large compared to the no-ARF scenario (solid black line in top graph of Fig. 3a), but relatively small among the two-layer scenarios (solid green, purple, and red line in top graph of Fig. 3a). This is a critical difference when a single

20 layer model is used (solid yellow lines in Fig. 3a). With only one layer, aerosol is distributed uniformly over the snowpack, and due to the scavenging ratio of 0.0, the total BC mass in the snow is conserved during the melt period. However, in contrast to the two-layer models, the BC concentration stays comparably low until shortly before meltout (solid yellow line in the center graph of Fig. 3a). Due to the uniform distribution of BC in the single layer model, a large fraction of the BC is located at depths where the radiative intensity is much lower than in the top few mm of the snowpack, leading to a weaker absorption efficiency.

25 This leads to a less pronounced decrease of albedo compared to the two layer models (solid yellow line in the top graph of Fig. 3a) and thus to a shorter meltout shift compared to a clean snowpack than in the 2-layer scenarios (about five days).

The sensitivity study using different values for the maximum surface layer thickness provides three important results. First, when the properties of the included LAISI are prone to melt amplification (scavenging ratio below 1), a minimum of two layers is required to simulate the effect of efficient absorption resulting from LAISI located close to the snow surface. Second,

30 the surface layer thickness only plays a minor role for the effect on the albedo, as long as the assumption that the surface layer thickness is much smaller than the penetration depth of shortwave radiation into the snowpack is justifiable. Third, by varying the surface layer thickness in a reasonable range, we cover a large range of BC increase in surface snow during melt, yet the effect on albedo, snow melt and snowpack evolution is minimal. Observed LAISI concentrations often are sampled in the top few centimetres of the snowpack and compared to surface layer concentration of models (e.g., Flanner et al., 2007;

35 Forsström et al., 2013), even though the surface layer is not a measurable snow property. Our results show that the comparison

of observed surface concentrations with simulations is critical due to the large impact of the model surface layer thickness on the surface concentration - while the effect on key snowpack variables such as the snow albedo remain nearly unaffected. This highlights the need for including a surface layer variation in the uncertainty estimation of the comparison with snow sampled in the surface layer.

5 5.1.2 Sensitivity to scavenging ratio of BC

Field measurements indicate that only a fraction of BC is flushed out with the melt water and BC can accumulate near the snow surface (e.g., Xu et al., 2012; Doherty et al., 2013; Sterle et al., 2013; Doherty et al., 2016). Our model is able to simulate this process by taking the scavenging ratio of BC during meltwater movement into account. In this section we explore the scavenging processes further, by investigating the impact of different BC scavenging ratios on the snowpack evolution.

10 Fig. 3b. In the range of investigated scavenging ratios, we find sensitivity of the BC surface mixing ratio, the albedo, and the subsequent snow melt to this parameter. When applying a melt scavenging factor typical for hydrophobic BC (green lines in graphs of Fig. 3b) there is little effect compared to the scenario without melt scavenging (purple lines; both show circa a factor 30 increase in surface BC concentration to the end of the melt season and only little differences in the development of albedo and snow melt). However, a distinction exists when using a scavenging ratio estimate for hydrophilic BC. In contrast to the no
15 melt scavenging and hydrophobic scenarios, surface BC does not increase as rapidly during the melt period (red line, central graph of Fig. 3b) and in fact is completely flushed when applying the max-estimate of hydrophilic scavenging (yellow line).

The changes in the scavenging ratio lead to a considerable effect on the albedo and the snow melt (meltout delayed by circa 1 (green lines), 2.5 (red lines), and 7 days (yellow lines) for scavenging ratios of 0.03, 0.2, and 2.0, respectively, compared to no melt scavenging (purple lines in Fig. 3b)). Compared to the no-ARF experiment (black lines), the presence of BC still
20 causes an earlier meltout of circa 8, 6.5, and 2 days for scavenging ratios of 0.03, 0.2, and 2.0, respectively, in our simulation. This implies a significant effect of BC on the albedo in all scenarios applied. Only when the melt scavenging is set to the upper limit (2.0; yellow lines in graphs of Fig. 3b), the surface concentration drops continuously during the melt period due to the highly efficient melt scavenging. As a consequence, the albedo converges against the albedo of the no-ARF case, before it drops roughly one day earlier to a value of circa 0.2 due to the earlier exposure of the underling ground (solid yellow and black
25 line in top graph of Fig. 3b). The slight increasing in difference in the melt rate between the no-ARF and the upper scavenging during the first 7 days of melt are due to the increasing absorption efficiency of BC with increasing optical snow grain size (e.g., Flanner et al., 2007). The following convergence (day 7 until 17 from melt onset) of both melt rates are due to the decreasing BC concentration in the upper scavenging scenario due to ongoing removal of BC (compare the dashed yellow and black line in top graph of Fig. 3b). However, even though nearly all BC is removed from the snow by the end of the melt period when
30 using the upper scavenging ratio, the melt out still happens circa two days earlier compared to the no-ARF experiment. This reveals that small amounts of BC in snow can impact the snowpack evolution over the whole melt period even under efficient scavenging.

5.1.3 Sensitivity to BC species

Hydrophilic BC absorbs stronger than hydrophobic BC under the same conditions due to an increased MAC compared to hydrophobic BC caused by the ageing of BC during atmospheric transport (Bond et al., 2006). On the other hand, as we previously explored, hydrophilic BC undergoes more efficient melt scavenging (Flanner et al., 2007), which impacts the snowpack evolution significantly. The column of graphs in Fig. 3c illustrates the net effect of these competing processes by applying the mid estimate of the scavenging ratio of hydrophobic BC (0.03) to both the hydrophobic BC (green curve) and the hydrophilic BC (purple curves) species. In this manner these curves show the isolated effect of the different absorption properties of the two species. We further apply the mid estimate for hydrophilic BC scavenging ratio (0.2) to hydrophilic BC (red curves) to quantify the gross effect. As in other cases, we include the no-ARF scenario (black curves) to highlight the overall effect on the albedo and melt of the different scenarios.

The isolated effect of the stronger absorption of hydrophilic BC leads to an earlier meltout by circa two days compared to hydrophobic BC (purple and green curves in graphs of Fig. 3c). However, when applying the mid estimate of the scavenging ratio for hydrophilic BC (0.2), the combined effects leads to a masking of the isolated effect of stronger absorption by hydrophilic BC (and vice versa). During the melt period, snow albedo, melt rate and the snowpack SWE barely differ between the scenarios with the mid estimate scavenging for hydrophobic and hydrophilic BC applied (red and green curves in top and bottom graphs of Fig. 3c). This reveals that both scenarios, hydrophobic BC with low scavenging efficiency and hydrophilic BC with high scavenging efficiency, lead roughly to an earlier meltout by circa 6 days. We interpret this that a clear distinction between the both species might play a secondary role in the determination of the overall impact of BC on snow melt.

5.1.4 Sensitivity to snowpack SWE at melt onset

In the following we explore the shortening of the melt period duration of snowpacks with constant BC mixing ratio at melt onset but different SWE relative to clean snowpacks with similar SWE. Results are shown in Fig. 4 for different scavenging ratios. Apart from SWE and scavenging ratio, all initial snowpack properties and the model input data are the same among the different scenarios, including an initial BC concentration of 35 ng g^{-1} . BC is distributed uniformly throughout the entire snowpack at melt onset. With respect to the range of snowpack SWE at melt onset presented here, the melt period shortening is stronger the smaller the scavenging ratio applied, and increasing with increasing SWE at melt onset. Results show a melt period reduction of up to 30% for the mid-estimate hydrophilic BC scavenging, end even higher when applying the mid-estimate hydrophobic BC scavenging.

With increasing SWE at melt onset, the increase in melt period shortening gets less pronounced (dashed and dashed-dotted curves in Fig. 4), and differences between the melt scavenging scenarios become larger. When applying very efficient melt scavenging (dotted curve in Fig. 4), the effect on the reduction is smallest over the range of SWE values shown, however, still leading to a melt period shortening between 4-8%.

The results suggest that not only the BC concentration and distribution, the snow properties, and the radiative properties and hydrophobicity of the aerosol control how BC in snow impacts the melt. The amount of snow accumulated also plays an

important role, with thicker snowpacks and similar LAISI mixing ratio at melt onset showing a stronger response to the LAISI induced processes.

5.2 Case study: Impact of BC deposition on the hydrology of a south Norwegian catchment

5.2.1 Performance of the model

5 In the split-sample test, the model performs reasonably well during both calibration and validation, with NSEs of 0.86 during the calibration period (green line in Fig. 5a) and 0.82 during the validation period (red line in Fig. 5a). However, in the winter season (circa November until March) the model generally underestimates the discharge and peaks in the beginning of the melt season are slightly underestimated. The scatter plot in Fig. 6 confirms the underestimation of low flow situations. For the case study analysis, we use model parameters from a calibration over the full period (1 September 2006 to 31 October 2012; 10 Fig. 5b), which results in a NSE of 0.84. We use mid-estimates for all LAISI-relevant parameters. The optimized parameters are listed in Table 2. Note that switching ARF off entirely (no BC deposition) leads to a slight decrease of the model quality (NSE of 0.83 over the whole period; not shown).

5.2.2 Evolution of surface BC mixing ratio

The evolution of surface albedo driven by BC deposition is distinct in the accumulation period vs. the melt period. During 15 the snow accumulation period (circa until end of March), only slight differences in albedo are noticeable. The average annual snow albedo from January 1st until March 22nd is 0.871 for the no-ARF experiment (Fig. 7a), while during the same time period, min, mid, and max scenarios show relative albedo reductions of 0.003, 0.010, and 0.014, respectively from the no-ARF case. The differences in snow albedo during the accumulation season are mostly due to differences in deposition and in the maximum surface layer thickness of the snowpack, and lead to average surface layer concentrations of 12, 49, and 98 ng g⁻¹ 20 (min, mid, and max estimates; Fig. 7b) at the beginning of the melt period.

With the start of the melt season, the difference in albedo is larger between model experiments. This has two reasons: (i) with increasing grain size during the melt season, the absorbing effect of BC gets more efficient due to deeper penetration of radiation into the snowpack leading to a stronger effect of the BC deposition on albedo (snow of larger grains has a larger extinction coefficient and more effective forward scattering properties (Flanner et al., 2007)). (ii) with the start of the melt 25 season there is a widespread decrease of snow thickness, allowing BC to accumulate in the surface layer. This latter effect is strongly depended on the applied scavenging ratios, as we demonstrated in the 1-D sensitivity study (cf. Sect. 5.1). During the melt season, the mid-scenario spatially averaged surface BC mixing ratio increases from 49 ng g⁻¹ to about 250 ng g⁻¹ (factor 5 increase) at the end of the melt season (beginning of July). For the max-scenario, the increase is from roughly 100 ng g⁻¹ to over 2500 ng g⁻¹ (factor 25 increase), while the min-scenario leads to a decrease in BC surface mixing ratio. At the end of the 30 melt season, the large differences in surface BC mixing ratio cause a relative decrease from the no-ARF case of about 0.03, 0.1 and over 0.3 for the min, mid, and max scenario, respectively.

For the min- and mid-scenario the model simulates an average annual surface BC mixing ratio of about 18 ng g^{-1} and 71 ng g^{-1} , respectively. Forsström et al. (2013) found for mainland Scandinavia values of the same magnitude, with seasonal means for different measurement locations and time periods ranging from about 10 ng g^{-1} to 80 ng g^{-1} . This places our results well within those presented in Forsström et al. (2013). Our max-scenario yields 198 ng g^{-1} which lies above average values expected from Forsström et al. (2013). However, Flanner et al. (2007) evaluated the global impact of the radiative forcing of BC in snow using a model which was compared with globally distributed surface BC measurements. For south Norway, Flanner et al. (2007) predicted an annual mean surface BC concentration between 46 and 215 ng g^{-1} for the year 1998. Including Flanner et al. (2007)'s results, our simulations reproduce a reasonable range of values.

Still, we recognize our max-scenario results in a strong increase in surface BC mixing ratios mostly due to low BC scavenging with melt (note the strong increase from end of March on in Fig. 7). This divergent evolution of surface BC mixing ratios in the min, mid, and max scenarios reveals uncertainty in the representation of the fate of BC in snow during melt. This uncertainty is also reflected in the literature. On the one hand, some studies report of high accumulation of BC in surface snow with implications for snow melt. Doherty et al. (2013) reported a factor 5 increase in surface BC mixing ratio under melt conditions, and in a subsequent study found increases of over an order of magnitude (Doherty et al., 2016). These findings were similar to Xu et al. (2012) who also found post-depositional enrichment of BC in surface snow over an order of magnitude. On the other hand, Lazarcik et al. (2017) observe efficiently scavenged BC, leading to decreased surface mixing ratios. In fact, they report BC leaching from the snow more rapidly than the snow melt and summarize that that surface enrichment of BC is not linked to SWE decreases during melt. The large differences in the evolution of surface BC mixing ratio during melt in our study reflects the range of uncertainties shown in previous studies. However, while the surface BC mixing ratio evolution during melt for min- and mid-scenario is within reason, it appears our max-scenario results in an overestimate of melt amplification.

5.2.3 BC induced radiative forcing

The radiative forcing in snow (RFS) induced by the presence of BC is calculated from the average radiative forcing over snow bearing tiles only. The RFS represents the additional uptake of energy from solar radiation per area snow cover due to the presence of BC in the snow compared to clean snow with the same properties. Fig. 8a shows the daily mean RFS and demonstrates the increase effect of RFS during snow melt. Low RFS is observed during the snow accumulation period then steadily increasing through spring snow melt, reaching values of approximately 8, 18, and 57 Wm^{-2} for the min, mid, and max scenarios, respectively (see red solid line and shaded area in Fig. 8a). The strong increase in RFS during spring melt results from the combination of: (i) the decrease in snow albedo due to the increase in surface BC concentrations (e.g. melt amplification and the increasing optical grain size in melting snow as discussed in Sect. 5.2.2) and, (ii) the increasing daily solar irradiation due to a lower solar zenith angle and longer days.

However, most relevant for discharge generation (see Sect. 5.2.4), is the catchment-wide total daily energy uptake due to BC, calculated as the mean radiative forcing over all grid cells. As the snow cover fraction (SCF) in the catchment drops during spring (dotted line and yellow shaded area in Fig. 7 and 8), the effect of the RFS on the melt generation is limited by the increasing area of bare ground. The net effect is shown in Fig. 8b. The catchment mean daily energy uptake due to the presence

of BC in snow shows a strong annual cycle and reaches a maximum of 1.3, 4.9, and 8.8 Wm^{-2} (min, mid, and max scenario, respectively) around the beginning of May. Radiative forcing in mid winter is small due low surface BC mixing ratios and low solar irradiate. (Qian et al., 2011) also reports a similar strong annual cycle with values in the same range for BC radiative forcing over the Tibetan Plateau using a global climate model, but with higher values in winter time. Annual mean values are 0.284, 0.844, and 1.391 Wm^{-2} for the min, mid, and max scenario. Averaged over entire Scandinavia (including Finland), Hienola et al. (2016) calculated lower values around 0.145 Wm^{-2} . However, Hienola et al. (2016) study includes large areas with shorter snow cover. Since the value is strongly depended on the snow cover evolution, higher values compared to Hienola et al. (2016) are expected due to the long lasting snow cover in our case study region.

5.2.4 BC impact on catchment discharge and snow storage

Fig. 9a shows the simulated daily discharge and catchment SWE averaged over the 6 years simulation period for the mid (red lines); min and max estimates (bounds of the shaded areas); and the no-ARF scenario (black lines). The differences in daily discharge and catchment SWE of the min, mid, and max scenarios to the no-ARF scenario are shown in Fig. 9b. All simulations with ARF show higher daily discharge from end of March until end of May and lower discharge from end of May until mid August relative to the no-ARF simulation. For the rest of the year, no effect on the discharge is noticeable. The net impact of RFS results in a shift in the timing of discharge. Higher discharge early in the melt season is observed, yet offset by lower discharge following May. The cumulative annual discharge remains nearly identical.

Min, mid, and max scenarios all show the change from higher to lower discharge compared to the no-ARF scenario approximately at the same time (at the end of May; see blue marker in Fig. 9b). Therefore, we can quantify the absolute and relative effect of RFS on the discharge during the two periods: the early melt season from circa March 22 until May 29 and the late melt season from circa May 30 until August 10 (Fig. 9b and see Table 3). This yields an average percentage increase in daily discharge of 2.5 %, 9.9 % and 21.4 % for the min, mid, and max scenario for the early melt season and a decrease in discharge of -0.8 %, -3.1 %, and -6.7 % during the late melt season.

The differences in discharge among the scenarios can be explained by understanding the evolution of the snowpack. In the all scenarios the catchment SWE (Fig. 9a) reaches a peak reduction relative to the no-ARF scenario of -4.6 %, -13.4 % and -34.4 % at mid May. The average difference in catchment SWE of the min, mid, and max scenarios compared to the no-ARF scenario during the entire melt season is -1.5, -5.1, and -10.3 mm; or an average of 2.1 %, 7.4 %, and 15.1 % (see Table 3). From mid May on, the differences in catchment SWE between scenarios drop continuously, which is equivalent to a higher catchment averaged snow melt rate in the no-ARF scenario compared to the ARF scenarios.

The difference at the beginning of the melt season can be attributed to RFS. However, from mid May on we see a decrease in the differences in catchment SWE between the ARF and no-ARF scenarios (Fig. 9b). To understand this counter-intuitive result, we need to evaluate the impact of BC deposition at the catchment scale. The dynamics driven by the SCF of the catchment is a limiting factor to the catchment averaged snow melt. Looking at Fig. 7a we see the development of average snow albedo and the SCF in the catchment. During the melt period, the catchment averaged albedo in all of the scenarios, decreases (and RFS is continually increasing). Intuitively, one would expect more melting due to enhanced solar radiative forcing. However, the SCF

decrease with increased melt due to ARF counteracts the RFS effect itself, due to the reduction in area from which snow can actually melt. This is also indicated in Fig. 8b, where the additional energy uptake due to BC in snow peaks in the beginning of May. We can see the same result for the discharge: the increased discharge of the ARF scenarios during the beginning of the melt season may simply be attributed to RFS, whereas the decreased discharge later in the season is attributed to melt limitation
5 caused by the SCF retreat.

Compared to observations, all simulations (ARF and no-ARF) tend to underestimate discharge during early melt season and overestimate discharge during late melt season (Fig. 9a). However, the magnitude of over- and underestimation strongly differs between the scenarios. By including ARF the volume error is reduced in both the early melt season (by increasing melt), and in late melt season (by subsequently decreasing melt generation in the catchment due to reduced SCF). Expressed as seasonal
10 mean volume error for early and late melt season, the difference to observed discharge is largest for the no-ARF scenario and smallest for max scenario. The max scenario reduces the volume error by -75.1% during early melt season and -89.9% during late melt season, relative to the no-ARF scenario (see Table 4). The min and mid scenarios also reduce the volume error. Thus, on average, an improvement in simulated discharge is achieved during the melt season by accounting for BC RFS.

5.3 Uncertainties

15 Both the literature and our analysis demonstrates numerous uncertainties and we urge further studies to address RFS-induced uncertainty. In our model study, uncertainties result principally from uncertainty of the mixing ratio of BC in the snowpack due to:

i) - prescribed BC deposition

In the approach presented here, we use prescribed BC deposition mass fluxes. Even though this is common practice (e.g.,
20 Goldenson et al., 2012; Lee et al., 2013; Jiao et al., 2014), it was showing by Doherty et al. (2014) that the decoupling of aerosol deposition from the water mass flux of falling snow can lead to an overestimation of surface mixing ratios by a factor of 1.5-2.5. However, we would like to highlight an important difference between our approach and the one (Doherty et al., 2014) claim to be problematic: First, the high bias in surface snow BC mixing ratios described by (Doherty et al., 2014) refers to global climate model simulations with prescribed aerosol deposition rates (wet and dry), where the input aerosol fields are
25 interpolated in time from monthly means. Therefore, the episodic nature of aerosol deposition due to wet deposition is generally absent in the prescribed-aerosol fields. The coupling of the interpolated fields with highly variable meteorology (in particular precipitation) results in the high bias (Doherty et al., 2014). In our case study, on the other hand, we use deposition fields originating from the regional aerosol climate model REMO-HAM, forced with ERA-Interim reanalysis data at the boundaries. REMO-HAM output is 3-hourly, which we re-sampled to daily means in order to have consistency between the deposition
30 fields and the observed daily precipitation used as input data in the hydrological simulations. The daily timestep allows us to preserve the episodic nature of aerosol deposition. Moreover, the daily BC wet deposition rates should not be biased due to major inaccuracies in precipitation as REMO-HAM has been shown to reproduce the Scandinavian precipitation realistically (Pietikäinen et al., 2012). The high bias occurring when using interpolated monthly averages as input should therefore be minimized.

Additionally, and significantly, (Doherty et al., 2014) (and the critiques therein) address an objective with consideration to climate impacts. Our analysis is focused on the impact to the hydrological cycle. Our simulations suggest that BC RFS is mostly important during spring time, where surface BC mixing ratio are predominantly controlled by melt processes, and not by deposition processes (as shown in Fig. 3 and Fig. 7b).

5 **ii) - LAISI other than BC**

By including only BC deposition in our simulation, we potentially underestimate the additional effect of further LAISI species such as mineral dust (Di Mauro et al., 2015; Painter et al., 2010), mixing of the snow with soil from the underlying ground, or local sources (Wang et al., 2013) and biological processes (Lutz et al., 2016). Neglecting additional RFS from LAISI other than BC is likely to result in an underestimation of the overall effect of LAISI on snow melt and discharge generation.

10 However, this implies that our approach gives a conservative estimate of the effect of LAISI, with BC being a proxy for the overall effect of LAISI on snow melt and discharge generation on the catchment scale.

6 **Conclusions**

Herein we presented a newly developed snow algorithm for application in hydrologic models that allows a new class of model input variables: the deposition rates of light absorbing aerosols. By coupling a radiative transfer model for snow to an energy
15 balance based snowpack model, we are providing a tool that can be used to determine the effect of various species of LAISI (herein shown for BC) on the hydrologic cycle at the catchment scale. From a 1-D model study, presented in Sect. 5.1, we conclude that:

i - the implementation of at least two layers (a thin surface layer and a bottom layer) is of outstanding importance to capture the potential effect of melt amplification on the near surface LAISI evolution. The maximum surface layer thickness
20 (in SWE) has a rather little effect on the snow albedo and melt rate as long as it is sufficiently small (smaller than the penetration depth of shortwave radiation). However, the evolution of the LAISI surface mixing ratio is highly sensitive to the maximum surface layer thickness. For this reason, we suggest to include a surface layer thickness variation in model studies when comparing simulated to observed LAISI mixing ratios sampled in the snow surface.

ii - The determination on how LAISI is washed out of the snowpack with melt water has great effect on the evolution of
25 LAISI concentration near the surface, snow albedo and melt rate. Due to rare observations of this effect the uncertainties are high and our findings show the need for more detailed understanding of the processes involved due to the high importance for the overall effect of LAISI in the snowpack.

iii - Snow rich areas are likely to be more effected by LAISI than areas with medium snow accumulation due to a nonlinear relationship between melt season duration and SWE at melt onset.

30 To prove the significance of the radiative forcing from BC for the hydrologic cycle at the catchment scale we demonstrated the effect of BC deposition and the subsequent implications for snow melt and discharge generation due to impacts on the snow

albedo on a remote mountain catchment. The study indicates that inclusion of BC in snow is likely to have a significant impact on melt timing, and that the effect on the discharge generation leads to a shift in the annual water balance. Our simulations further suggest that melt amplification can have severe implications on the impact of BC on both, the snowpack evolution and the discharge regime of a catchment, which means that the seasonal cycle of surface BC mixing ratio is of great importance.

5 However, large uncertainties are connected with the representation of surface enrichment of BC. Especially for the impact on the hydrological cycle, the fate of the BC in melting snow is essential.

Including radiative forcing from BC in the simulations leads to a reduction in volume error during the early and late melt season in our simulations. We conclude from our study that hydrological modelling can potentially be improved by including the effect of LAISI, especially when the model approach implicates a physically based representation of the snowpack in
10 general and the snow albedo in particular. However, more research in the area of catchment scale impact of LAISI is needed to support this. The model tool presented in this study allows to target this in future applications.

Acknowledgements. This work was conducted within the Norwegian Research Council's INDNOR program under the Hydrologic sensitivity to Cryosphere-Aerosol interaction in Mountain Processes (HyCAMP) project (NFR no. 222195). We thank the Mitigation of Arctic warming by controlling European black carbon emissions (MACEB) project for their help concerning the REMO-HAM simulations. Furthermore, we
15 thank the International Institute for Applied System Analysis (IIASA), especially Kaarle Kupiainen and Zbigniew Klimont, for providing the the emissions data. Sigbjorn Helset and Statkraft AS, in general, have been vital resources in the development of the algorithm and, in particular, the implmentation into Shyft. The ECHAM-HAMMOZ model is developed by a consortium composed of ETH Zurich, Max Planck Institut für Meteorologie, Forschungszentrum Jülich, University of Oxford, and the Finnish Meteorological Institute and managed by the Center for Climate Systems Modeling (C2SM) at ETH Zurich. We also would like to thank Sigbjørn Helseth from Statkraft for the
20 support during the implementation of our algorithm into the Shyft framework.

References

- Aas, K. S., Gislås, K., Westermann, S., and Berntsen, T. K.: A Tiling Approach to Represent Subgrid Snow Variability in Coupled Land Surface–Atmosphere Models, *Journal of Hydrometeorology*, 18, 49–63, doi:10.1175/JHM-D-16-0026.1, 2017.
- AMAP, .: AMAP Assessment 2015: Black carbon and ozone as Arctic climate forcers, Arctic Monitoring and Assessment Programme (AMAP), 2015.
- Anderson, E. A.: A Point Energy and Mass Balance Model of a Snow Cover, NOAA Technical Report NWS, 19, 1976.
- Berghuijs, W. R., Woods, R. A., Hutton, C. J., and Sivapalan, M.: Dominant flood generating mechanisms across the United States, *Geophysical Research Letters*, 43, 4382–4390, doi:10.1002/2016GL068070, 2016.
- Bond, T. C., Habib, G., and Bergstrom, R. W.: Limitations in the enhancement of visible light absorption due to mixing state, *Journal of Geophysical Research*, 111, D20211, doi:10.1029/2006JD007315, 2006.
- Bond, T. C., Doherty, S. J., Fahey, D. W., Forster, P. M., Berntsen, T., DeAngelo, B. J., Flanner, M. G., Ghan, S., Kärcher, B., Koch, D., Kinne, S., Kondo, Y., Quinn, P. K., Sarofim, M. C., Schultz, M. G., Schulz, M., Venkataraman, C., Zhang, H., Zhang, S., Bellouin, N., Guttikunda, S. K., Hopke, P. K., Jacobson, M. Z., Kaiser, J. W., Klimont, Z., Lohmann, U., Schwarz, J. P., Shindell, D., Storelvmo, T., Warren, S. G., and Zender, C. S.: Bounding the role of black carbon in the climate system: A scientific assessment, *Journal of Geophysical Research: Atmospheres*, 118, 5380–5552, doi:10.1002/jgrd.50171, 2013.
- Brun, E.: Investigation on wet-snow metamorphisms in respect of liquid water content, *Annals of Glaciology*, 13, 1989.
- Bryant, A. C., Painter, T. H., Deems, J. S., and Bender, S. M.: Impact of dust radiative forcing in snow on accuracy of operational runoff prediction in the Upper Colorado River Basin, *Geophysical Research Letters*, 40, 3945–3949, doi:10.1002/grl.50773, 2013.
- Conway, H., Gades, A., and Raymond, C. F.: Albedo of dirty snow during conditions of melt, *Water Resources Research*, 32, 1713–1718, 1996.
- Dee, D. P., Uppala, S. M., Simmons, A. J., Berrisford, P., Poli, P., Kobayashi, S., Andrae, U., Balmaseda, M. A., Balsamo, G., Bauer, P., Bechtold, P., Beljaars, A. C. M., van de Berg, L., Bidlot, J., Bormann, N., Delsol, C., Dragani, R., Fuentes, M., Geer, A. J., Haimberger, L., Healy, S. B., Hersbach, H., Hólm, E. V., Isaksen, I., Kållberg, P., Köhler, M., Matricardi, M., McNally, A. P., Monge-Sanz, B. M., Morcrette, J.-J., Park, B.-K., Peubey, C., de Rosnay, P., Tavolato, C., Thépaut, J.-N., and Vitart, F.: The ERA-Interim reanalysis: configuration and performance of the data assimilation system, *Quarterly Journal of the Royal Meteorological Society*, 137, 553–597, doi:10.1002/qj.828, 2011.
- Dentener, F., Kinne, S., Bond, T., Boucher, O., Cofala, J., Generoso, S., Ginoux, P., Gong, S., Hoelzemann, J. J., Ito, A., Marelli, L., Penner, J. E., Putaud, J.-P., Textor, C., Schulz, M., van der Werf, G. R., and Wilson, J.: Emissions of primary aerosol and precursor gases in the years 2000 and 1750 prescribed data-sets for AeroCom, *Atmospheric Chemistry and Physics*, 6, 4321–4344, doi:10.1029/2003JD003697,, 2006.
- Di Mauro, B., Fava, F., Ferrero, L., Garzonio, R., Baccolo, G., Delmonte, B., and Colombo, R.: Mineral dust impact on snow radiative properties in the European Alps combining ground, UAV, and satellite observations, *Journal of Geophysical Research: Atmospheres*, 120, 6080–6097, doi:10.1002/2015JD023287, 2015.
- Diggle, P. J. and Ribeiro, P. J.: *Model-based Geostatistics*, Springer Series in Statistics, Springer, New York, USA, 2007.
- Doherty, S. J., Grenfell, T. C., Forsström, S., Hegg, D. L., Brandt, R. E., and Warren, S. G.: Observed vertical redistribution of black carbon and other insoluble light-absorbing particles in melting snow, *Journal of Geophysical Research: Atmospheres*, 118, 5553–5569, doi:10.1002/jgrd.50235, 2013.

- Doherty, S. J., Bitz, C. M., and Flanner, M. G.: Biases in modeled surface snow BC mixing ratios in prescribed-aerosol climate model runs, *Atmospheric Chemistry and Physics*, 14, 11 697–11 709, doi:10.5194/acp-14-11697-2014, 2014.
- Doherty, S. J., Hegg, D. A., Johnson, J. E., Quinn, P. K., Schwarz, J. P., Dang, C., and Warren, S. G.: Causes of variability in light absorption by particles in snow at sites in Idaho and Utah, *Journal of Geophysical Research: Atmospheres*, 121, 4751–4768, doi:10.1002/2015JD024375, 5 2016.
- Domine, F., Taillandier, A.-S., and Simpson, W. R.: A parameterization of the specific surface area of seasonal snow for field use and for models of snowpack evolution, *Journal of Geophysical Research: Earth Surface*, 112, F02 031, doi:10.1029/2006JF000512, 2007.
- Engelhardt, M., Schuler, T. V., and Andreassen, L. M.: Contribution of snow and glacier melt to discharge for highly glacierised catchments in Norway, *Hydrology and Earth System Sciences*, 18, 511–523, doi:10.5194/hess-18-511-2014, 2014.
- 10 Flanner, M. G. and Zender, C. S.: Linking snowpack microphysics and albedo evolution, *Journal of Geophysical Research: Atmospheres*, 111, D12 208, doi:10.1029/2005JD006834, 2006.
- Flanner, M. G., Zender, C. S., Randerson, J. T., and Rasch, P. J.: Present-day climate forcing and response from black carbon in snow, *Journal of Geophysical Research: Atmospheres*, 112, D11 202, doi:10.1029/2006JD008003, 2007.
- Flanner, M. G., Zender, C. S., Hess, P. G., Mahowald, N. M., Painter, T. H., Ramanathan, V., and Rasch, P. J.: Springtime warming and reduced 15 snow cover from carbonaceous particles, *Atmospheric Chemistry and Physics*, 9, 2481– 2497, doi:10.1029/2005JD006356., 2009.
- Forsström, S., Isaksson, E., Skeie, R. B., Ström, J., Pedersen, C. A., Hudson, S. R., Berntsen, T. K., Lihavainen, H., Godtliebsen, F., and Gerland, S.: Elemental carbon measurements in European Arctic snow packs, *Journal of Geophysical Research: Atmospheres*, 118, 13,614–13,627, doi:10.1002/2013JD019886, 2013.
- Førland, E. J.: Nedbørens høydeavhengighet (Precipitation and topography, in Norwegian with English summary), *Klima*, 1, 3–24, 1979.
- 20 Gislås, K., Westermann, S., Schuler, T. V., Melvold, K., and Etzelmüller, B.: Small-scale variation of snow in a regional permafrost model, *The Cryosphere*, 10, 1201–1215, doi:10.5194/tc-10-1201-2016, 2016.
- Goldenson, N., Doherty, S. J., Bitz, C. M., Holland, M. M., Light, B., and Conley, A. J.: Arctic climate response to forcing from light-absorbing particles in snow and sea ice in CESM, *Atmospheric Chemistry and Physics*, 12, 7903–7920, doi:10.5194/acp-12-7903-2012, 2012.
- 25 Hartmann, M. D., Baron, J. S., Lammers, R. B., Cline, D. W., Band, L. E., Liston, G. E., and Tague, C.: Simulations of snow distribution and hydrology in a mountain basin, *Water Resources Research*, 35, 1587–1603, 1999.
- Hegdahl, T. J., Tallaksen, L. M., Engeland, K., Burkhart, J. F., and Xu, C.-Y.: Discharge sensitivity to snowmelt parameterization: a case study for Upper Beas basin in Himachal Pradesh, India, *Hydrology Research*, 47, 683–700, doi:10.2166/nh.2016.047, 2016.
- Hienola, A. I., Pietikäinen, J.-P., Jacob, D., Pozdun, R., Petäjä, T., Hyvärinen, A.-P., Sogacheva, L., Kerminen, V.-M., Kulmala, M., and 30 Laaksonen, A.: Black carbon concentration and deposition estimations in Finland by the regional aerosol–climate model REMO-HAM, *Atmospheric Chemistry and Physics*, 13, 4033–4055, doi:10.5194/acp-13-4033-2013, 2013.
- Hienola, A. I., O’Donnell, D., Pietikäinen, J.-P., Svensson, J., Lihavainen, H., Virkula, A., Korhonen, H., and Laaksonen, A.: The radiative impact of Nordic anthropogenic black carbon, *Tellus B*, 68, doi:10.3402/tellusb.v68.27428, 2016.
- Jacobson, M. Z.: Climate response of fossil fuel and biofuel soot, accounting for soot’s feedback to snow and sea ice albedo and emissivity, 35 *Journal of Geophysical Research: Atmospheres*, 109, n/a–n/a, doi:10.1029/2004JD004945, 2004.
- Jeelani, G., Feddema, J. J., van der Veen, C. J., and Stearns, L.: Role of snow and glacier melt in controlling river hydrology in Liddar watershed (western Himalaya) under current and future climate, *Water Resources Research*, 48, n/a–n/a, doi:10.1029/2011WR011590, 2012.

- Jiao, C., Flanner, M. G., Balkanski, Y., Bauer, S. E., Bellouin, N., Berntsen, T. K., Bian, H., Carslaw, K. S., Chin, M., De Luca, N., Diehl, T., Ghan, S. J., Iversen, T., Kirkevåg, A., Koch, D., Liu, X., Mann, G. W., Penner, J. E., Pitari, G., Schulz, M., Seland, O., Skeie, R. B., Steenrod, S. D., Stier, P., Takemura, T., Tsigaridis, K., van Noije, T., Yun, Y., and Zhang, K.: An AeroCom assessment of black carbon in Arctic snow and sea ice, *Atmospheric Chemistry and Physics*, 14, 2399–2417, doi:10.5194/acp-14-2399-2014, 2014.
- 5 Jonas, T., Rixen, C., Sturm, M., and Stoeckli, V.: How alpine plant growth is linked to snow cover and climate variability, *Journal of Geophysical Research*, 113, G03 013, doi:10.1029/2007JG000680, 2008.
- Junghans, N., Cullmann, J., and Huss, M.: Evaluating the effect of snow and ice melt in an Alpine headwater catchment and further downstream in the River Rhine, *Hydrological Sciences Journal*, 56, 981–993, doi:10.1080/02626667.2011.595372, 2011.
- Kaspari, S., McKenzie Skiles, S., Delaney, I., Dixon, D., and Painter, T. H.: Accelerated glacier melt on Snow Dome, Mount Olympus, Washington, USA, due to deposition of black carbon and mineral dust from wildfire, *Journal of Geophysical Research: Atmospheres*, 120, 2793–2807, doi:10.1002/2014JD022676, 2015.
- 10 Kawagoe, S., Kazama, S., and Ranjan Sarukkalige, P.: Assessment of snowmelt triggered landslide hazard and risk in Japan, *Cold Regions Science and Technology*, 58, 120–129, doi:10.1016/j.coldregions.2009.05.004, 2009.
- Kirchner, J. W.: Catchments as simple dynamical systems: Catchment characterization, rainfall-runoff modeling, and doing hydrology backward, *Water Resources Research*, 45, W2429, doi:10.1029/2008WR006912, 2009.
- 15 Klemes, V.: Operational testing of hydrological simulation models, *Hydrological Sciences Journal*, 31, 13–24, doi:10.1080/02626668609491024, 1986.
- Klimont, Z., Höglund-Isaksson, L., Heyes, C., Rafaj, P., Schöpp, W., Cofala, J., Borcken-Kleefeld, J., Purohit, P., Kupiainen, K., Winiwarter, W., Amann, M., Zhao, B., Wang, S., Bertok, I., and Sander, R.: Global scenarios of air pollutants and methane: 1990-2050, In preparation, 2016a.
- 20 Klimont, Z., Kupiainen, K., Heyes, C., Purohit, P., Cofala, J., Rafaj, P., Borcken-Kleefeld, J., and Schöpp, W.: Global anthropogenic emissions of particulate matter including black carbon, *Atmospheric Chemistry and Physics Discussions*, pp. 1–72, doi:10.5194/acp-2016-880, 2016b.
- Kolberg, S. and Gottschalk, L.: Interannual stability of grid cell snow depletion curves as estimated from MODIS images, *Water Resources Research*, 46, W11 555, doi:10.1029/2008WR007617, 2010.
- 25 Krinner, G., Boucher, O., and Balkanski, Y.: Ice-free glacial northern Asia due to dust deposition on snow, *Climate Dynamics*, 27, 613–625, doi:10.1007/s00382-006-0159-z, 2006.
- Lazarcik, J., Dibb, J. E., Adolph, A. C., Amante, J. M., Wake, C. P., Scheuer, E., Mineau, M. M., and Albert, M. R.: Major fraction of black carbon is flushed from the melting New Hampshire snowpack nearly as quickly as soluble impurities, *Journal of Geophysical Research: Atmospheres*, 122, 537–553, doi:10.1002/2016JD025351, 2017.
- 30 Lee, Y. H., Lamarque, J.-F., Flanner, M. G., Jiao, C., Shindell, D. T., Berntsen, T., Bisiaux, M. M., Cao, J., Collins, W. J., Curran, M., Edwards, R., Faluvegi, G., Ghan, S., Horowitz, L. W., McConnell, J. R., Ming, J., Myhre, G., Nagashima, T., Naik, V., Rumbold, S. T., Skeie, R. B., Sudo, K., Takemura, T., Thevenon, F., Xu, B., and Yoon, J.-H.: Evaluation of preindustrial to present-day black carbon and its albedo forcing from Atmospheric Chemistry and Climate Model Intercomparison Project (ACCMIP), *Atmospheric Chemistry and Physics*, 13, 2607–2634, doi:10.5194/acp-13-2607-2013, 2013.
- 35 Liston, G. E.: Representing Subgrid Snow Cover Heterogeneities in Regional and Global Models, *Journal of Climate*, 17, 1381 – 1397, 2004.
- Luce, C. H. and Tarboton, D. G.: The application of depletion curves for parameterization of subgrid variability of snow, *Hydrological Processes*, 18, 1409–1422, doi:10.1002/hyp.1420, 2004.

- Lutz, S., Anesio, A. M., Raiswell, R., Edwards, A., Newton, R. J., Gill, F., and Benning, L. G.: The biogeography of red snow microbiomes and their role in melting arctic glaciers, *Nature Communications*, 7, 11 968, doi:10.1038/ncomms11968, 2016.
- Melvold, K. and Skaugen, T.: Multiscale spatial variability of lidar-derived and modeled snow depth on Hardangervidda, Norway, *Annals of Glaciology*, 54, 273–281, doi:10.3189/2013AoG62A161, 2013.
- 5 Oaida, C. M., Xue, Y., Flanner, M. G., Skiles, S. M., De Sales, F., and Painter, T. H.: Improving snow albedo processes in WRF/SSiB regional climate model to assess impact of dust and black carbon in snow on surface energy balance and hydrology over western U.S., *Journal of Geophysical Research: Atmospheres*, 120, 3228–3248, doi:10.1002/2014JD022444, 2015.
- Painter, T. H., Barrett, A. P., Landry, C. C., Neff, J. C., Cassidy, M. P., Lawrence, C. R., McBride, K. E., and Farmer, G. L.: Impact of disturbed desert soils on duration of mountain snow cover, *Geophysical Research Letters*, 34, L12 502, doi:10.1029/2007GL030284, 2007.
- 10 Painter, T. H., Deems, J. S., Belnap, J., Hamlet, A. F., Landry, C. C., and Udall, B.: Response of Colorado River runoff to dust radiative forcing in snow, *Proceedings of the National Academy of Sciences of the United States of America*, 107, 17 125–17 130, doi:10.1073/pnas.0913139107/-DCSupplemental, 2010.
- Painter, T. H., Skiles, S. M., Deems, J. S., Bryant, A. C., and Landry, C. C.: Dust radiative forcing in snow of the Upper Colorado River Basin: 1. A 6 year record of energy balance, radiation, and dust concentrations, *Water Resources Research*, 48, n/a–n/a, doi:10.1029/2012WR011985, 2012.
- 15 Pietikäinen, J.-P., O'Donnell, D., Teichmann, C., Karstens, U., Pfeifer, S., Kazil, J., Podzun, R., Fiedler, S., Kokkola, H., Birmili, W., O'Dowd, C., Baltensperger, U., Weingartner, E., Gehrig, R., Spindler, G., Kulmala, M., Feichter, J., Jacob, D., and Laaksonen, A.: The regional aerosol-climate model REMO-HAM, *Geoscientific Model Development*, 5, 1323–1339, doi:10.5194/gmd-5-1323-2012, 2012.
- Pietikäinen, J.-P., Kupiainen, K., Klimont, Z., Makkonen, R., Korhonen, H., Karinkanta, R., Hyvärinen, A.-P., Karvosenoja, N., Laaksonen, A., Lihavainen, H., and Kerminen, V.-M.: Impacts of emission reductions on aerosol radiative effects, *Atmospheric Chemistry and Physics*, 20 15, 5501–5519, doi:10.5194/acp-15-5501-2015, 2015.
- Powell, M.: The BOBYQA algorithm for bound constrained optimization without derivatives, 2009.
- Priestley, C. H. B. and Taylor, R. J.: On the assessment of surface heat flux and evaporation using large-scale parameters, *Monthly Weather Review*, 100, 81–92, 1972.
- 25 Qian, Y., Gustafson, W. I., Leung, L. R., and Ghan, S. J.: Effects of soot-induced snow albedo change on snowpack and hydrological cycle in western United States based on Weather Research and Forecasting chemistry and regional climate simulations, *Journal of Geophysical Research: Atmospheres*, 114, D03 108, doi:10.1029/2008JD011039, 2009.
- Qian, Y., Flanner, M. G., Leung, L. R., and Wang, W.: Sensitivity studies on the impacts of Tibetan Plateau snowpack pollution on the Asian hydrological cycle and monsoon climate, *Atmospheric Chemistry and Physics*, 11, 1929–1948, doi:10.5194/acp-11-1929-2011, 2011.
- 30 Rhodes, J. J., Armstrong, R. L., and Warren, S. G.: Mode of formation of "ablation hollows" controlled by dirt content of snow, *Journal of Glaciology*, 33, 135–139, 1987.
- Roy, A., Royer, A., Montpetit, B., Bartlett, P. A., and Langlois, A.: Snow specific surface area simulation using the one-layer snow model in the Canadian LAnd Surface Scheme (CLASS), *The Cryosphere*, 7, 961–975, doi:10.5194/tc-7-961-2013, 2013.
- Skiles, S. M., Painter, T. H., Deems, J. S., Bryant, A. C., and Landry, C. C.: Dust radiative forcing in snow of the Upper Colorado River Basin: 2. Interannual variability in radiative forcing and snowmelt rates, *Water Resources Research*, 48, W07 522, doi:10.1029/2012WR011986, 2012.
- 35 Sterle, K. M., McConnell, J. R., Dozier, J., Edwards, R., and Flanner, M. G.: Retention and radiative forcing of black carbon in eastern Sierra Nevada snow, *The Cryosphere*, 7, 365–374, doi:10.5194/tc-7-365-2013, 2013.

- Stier, P., Feichter, J., Kinne, S., Kloster, S., Vignati, E., Wilson, J., Ganzeveld, L., Tegen, I., Werner, M., Balkanski, Y., Schulz, M., Boucher, O., Minikin, A., and Petzold, A.: The aerosol-climate model ECHAM5-HAM, *Atmospheric Chemistry and Physics*, 5, 1125–1156, doi:10.1029/2001JD001, 2005.
- Taillandier, A.-S., Domine, F., Simpson, W. R., Sturm, M., and Douglas, T. A.: Rate of decrease of the specific surface area of dry snow: Isothermal and temperature gradient conditions, *Journal of Geophysical Research*, 112, F03 003, doi:10.1029/2006JF000514, 2007.
- Toon, O. B., McKay, C. P., and Ackerman, T. P.: Rapid Calculation of Radiative Heating Rates and Photodissociation Rates in Inhomogeneous Multiple Scattering Atmospheres, *Journal of Geophysical Research*, 94, 16,287–16,301, 1989.
- van der Werf, G. R., Randerson, J. T., Giglio, L., Collatz, G. J., Mu, M., Kasibhatla, P. S., Morton, D. C., DeFries, R. S., Jin, Y., and van Leeuwen, T. T.: Global fire emissions and the contribution of deforestation, savanna, forest, agricultural, and peat fires (1997–2009), *Atmospheric Chemistry and Physics*, 10, 11 707–11 735, doi:10.5194/acp-10-11707-2010, 2010.
- Wang, X., Doherty, S. J., and Huang, J.: Black carbon and other light-absorbing impurities in snow across Northern China, *Journal of Geophysical Research: Atmospheres*, 118, 1471–1492, doi:10.1029/2012JD018291, 2013.
- Warren, S. G. and Wiscombe, W. J.: A Model for the Spectral Albedo of Snow. II: Snow Containing Atmospheric Aerosols, *Journal of the Atmospheric Sciences*, 37, 2734–2745, 1980.
- Weedon, G. P., Balsamo, G., Bellouin, N., Gomes, S., Best, M. J., and Viterbo, P.: The WFDEI meteorological forcing data set: WATCH Forcing Data methodology applied to ERA-Interim reanalysis data, *Water Resources Research*, 50, 7505–7514, doi:10.1002/2014WR015638, 2014.
- Winstral, A. and Marks, D.: Simulating wind fields and snow redistribution using terrain-based parameters to model snow accumulation and melt over a semi-arid mountain catchment, *Hydrological Processes*, 16, 3585–3603, doi:10.1002/hyp.1238, 2002.
- Wiscombe, W. J. and Warren, S. G.: A Model for the Spectral Albedo of Snow. I: Pure Snow, *Journal of the Atmospheric Sciences*, 37, 2712–2733, 1980.
- Xu, B., Cao, J., Joswiak, D. R., Liu, X., Zhao, H., and He, J.: Post-depositional enrichment of black soot in snow-pack and accelerated melting of Tibetan glaciers, *Environmental Research Letters*, 7, 014 022, doi:10.1088/1748-9326/7/1/014022, 2012.
- Zhang, K., O'Donnell, D., Kazil, J., Stier, P., Kinne, S., Lohmann, U., Ferrachat, S., Croft, B., Quaas, J., Wan, H., Rast, S., and Feichter, J.: The global aerosol-climate model ECHAM-HAM, version 2: sensitivity to improvements in process representations, *Atmospheric Chemistry and Physics*, 12, 8911–8949, doi:10.5194/acp-12-8911-2012, 2012.

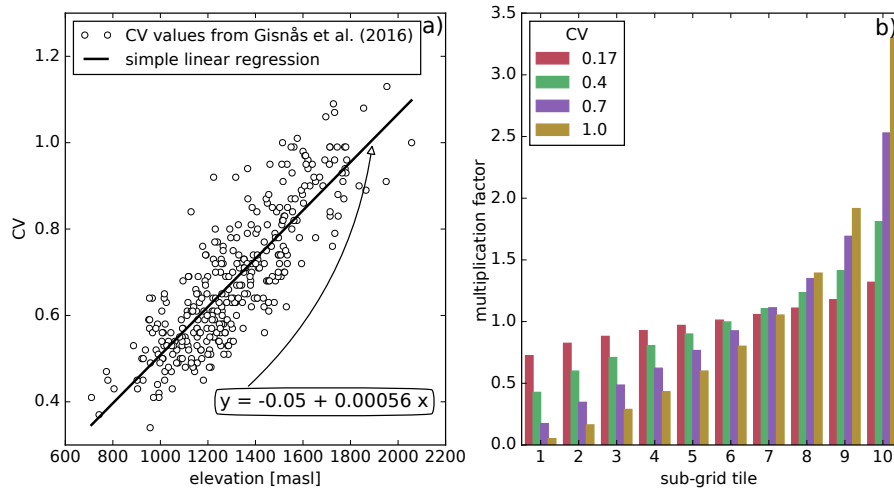


Figure 1. Left: elevation versus coefficients of variation (CV) of sub-grid snow distribution from Gislås et al. (2016) of forest free areas in the Atnsjoen catchment (dots) and the relationship between the CVs and the elevation resulting from simple linear regression analysis (black line). Right: solid precipitation multiplication factors for the sub-grid snow tiles for different CVs.

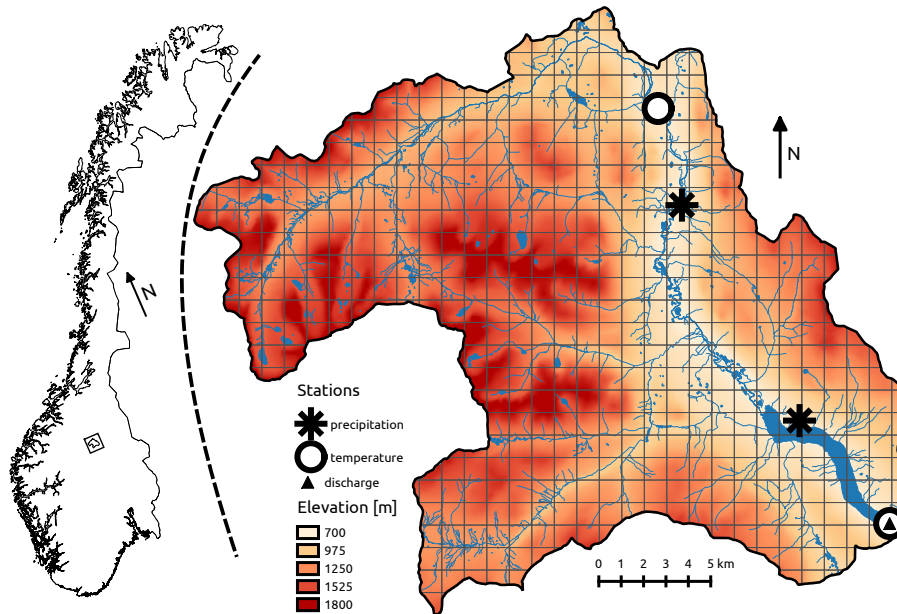


Figure 2. Location of the Atnsjoen catchment in Norway (black box in left map) and overview map of the Atnsjoen catchment (right).

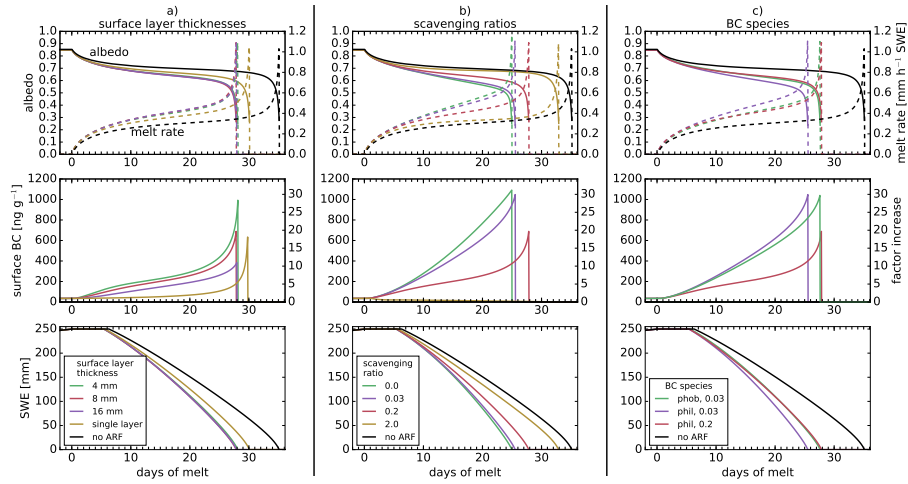


Figure 3. Snow albedo (top row of graphs; solid lines) and melt rate (top row of graphs; dashed lines), BC mixing ratio in the surface layer and factor increase of the mixing ratio during melt compared to the pre-melt BC mixing ratio (central row of graphs), and snowpack SWE (bottom row of graphs) for simulations forced with synthetic data based on the average meteorological conditions during the melt season from mid March until mid July of the Atnsjoen catchment and different model configurations: (a) different values for maximum surface layer thickness; (b) scavenging ratio; and (c) BC species with different melt scavenging ratios applied (*phob* and *phil* in legend stands for hydrophobic and hydrophilic BC, respectively). The black lines in all graph show simulation results of model runs without ARF applied (no-ARF).

Table 1. Information about observational stations.

Station name	Station ID	Operator	Observational variable	Elevation
Atnsjoen 1	8720	MET	precipitation	749
Atndalen-Eriksrud	8770	MET	precipitation	731
Atnsjoen 2	2.32.0	NVE	temperature	701
Li Bru	2.479.0	NVE	temperature	780
Fokstuga	16610	MET	wind speed; relative humidity	973
Kvitfjell	13160	MET	wind speed	1030
Venabu	13420	MET	relative humidity	930

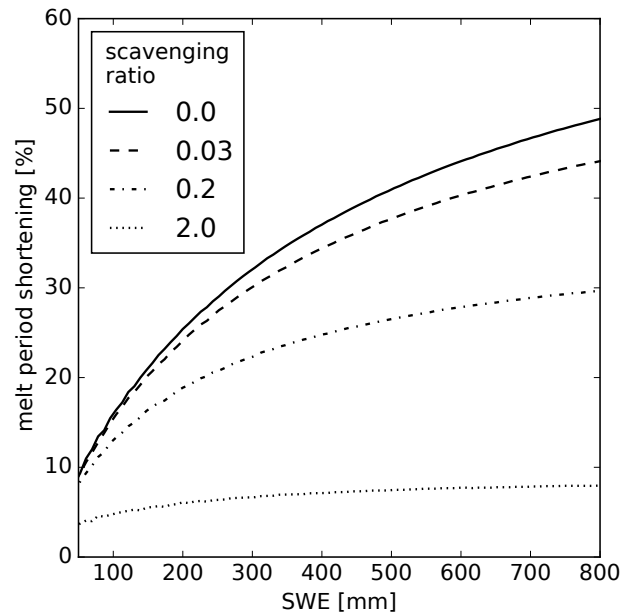


Figure 4. Shortening of the melt period duration for simulations with different SWE at melt onset relative to the simulations without ARF. Uniform BC mixing ratio in the snowpack is 35 ng g^{-1} at melt onset.

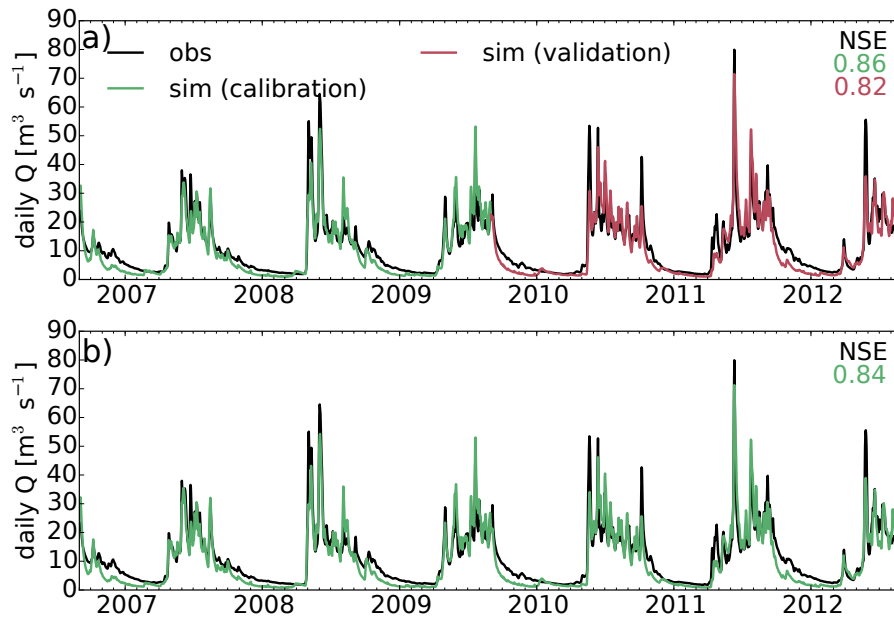


Figure 5. Simulated (green and red curves) and observed (black curve) daily discharge from the Atnsjoen watershed. Graph (a) is showing the simulation results for 3 years of calibration (green) and 3 years of validation (red). Graph (b) is showing the results for the 6 years calibration period. Parameters estimated in the latter are used in the case study. Parameters not included in the optimization are set to mid-estimate values during the calibration process (see Table 2).

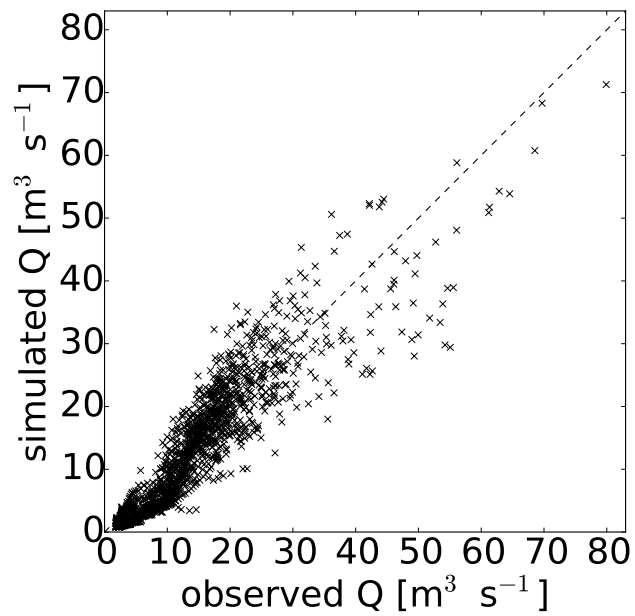


Figure 6. Comparison of observed and simulated daily discharge Q of the Atnsjoen catchment. The dashed black line demonstrates perfect agreement between simulation and observation.

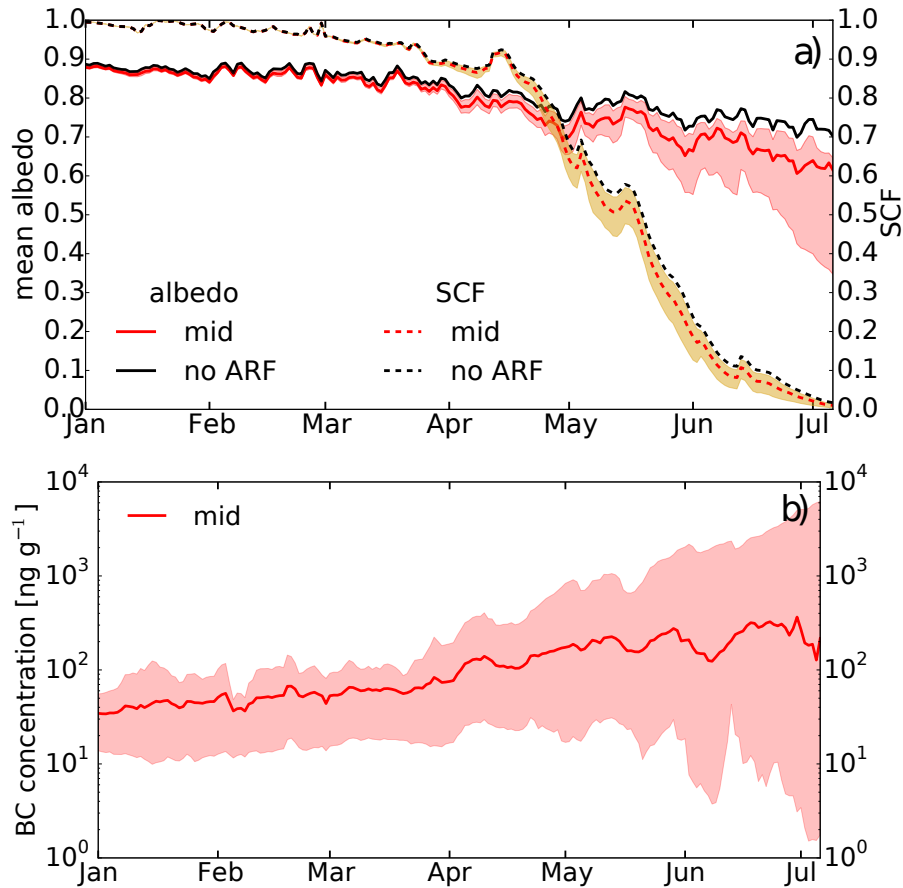


Figure 7. (a) Simulated mean catchment snow albedo (solid lines) and snow covered fraction (SCF; dashed lines) for the mid (red lines), low and high (shaded) estimates and for the scenario without ARF (no-ARF; black lines) averaged over the 6 years period. (b) Concentration of BC in the surface layer of the model for the mid (solid line), min (lower bound of shaded area) and max (upper bound of shaded area) estimates.

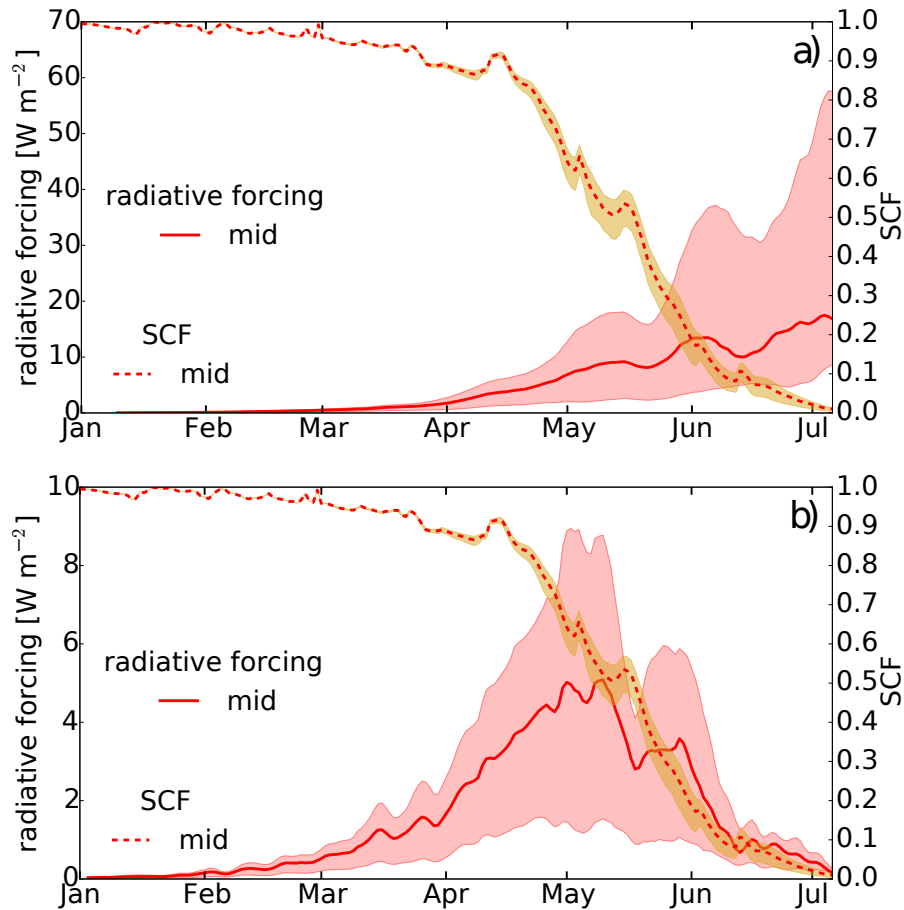


Figure 8. Catchment snow covered fraction (SCF; dashed lines) and (a) simulated mean radiative forcing in snow and (b) total daily energy uptake in the catchment due to BC for the mid (solid red lines), min (lower bound of shaded area) and max (upper bound of shaded area) estimates averaged over the 6 years period (daily means presented in Watts per square meter catchment area).

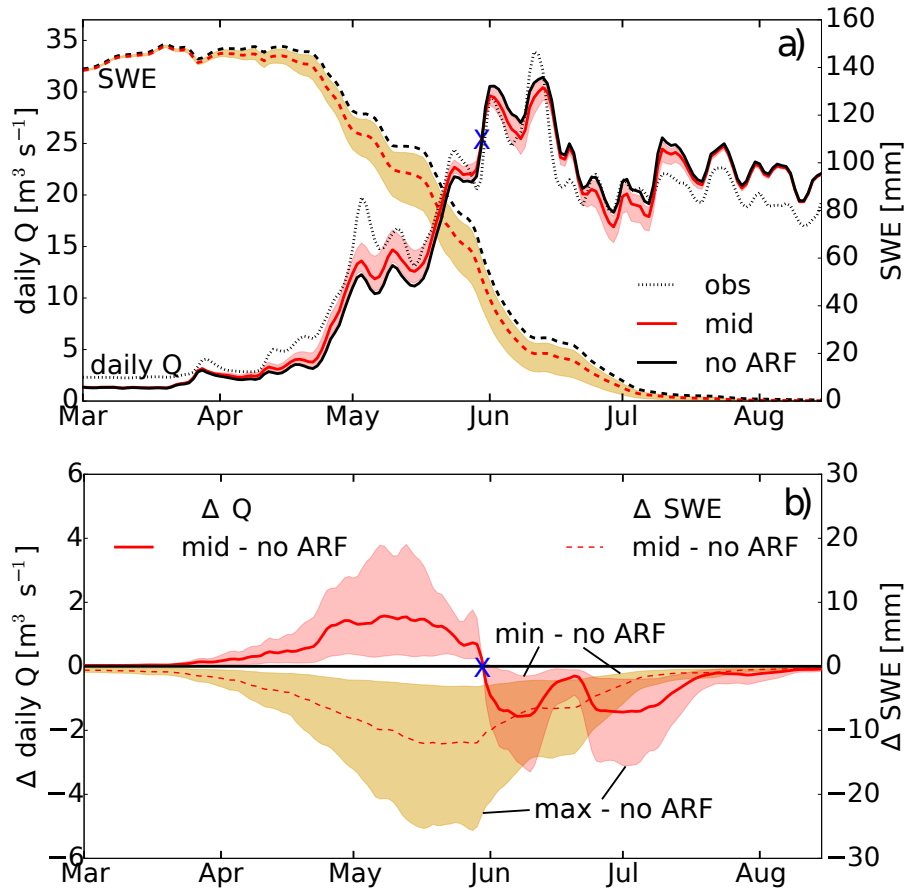


Figure 9. (a) Simulated daily discharge (Q; solid lines) and catchment mean snow water equivalent (SWE; dashed lines) for the mid (red lines), low and high (shaded) estimates and for the scenario without ARF (no-ARF; black lines) averaged over the 6 years period. (b) Differences in daily discharge and SWE of ARF scenarios to the scenario without ARF (no-ARF). The blue marker in (a) and (b) separates the periods where BC in snow has an enhancing (left of marker) and a decreasing (right of marker) effect on the discharge.

Table 2. Model parameters used in sensitivity and case study. Parameters optimized during calibration are marked with *. Further parameters were pre-set and not open for calibration. Parameters with different values in the minimum (min), central (mid), and maximum (max) BC radiative forcing estimates are marked with **.

Parameter	Description and unit	min estimate	optimized/set mid estimate	max estimate
c_1 *	kirchner parameter 1 (see Eq. 3) [-]		-4.298	
c_2 *	kirchner parameter 2 (see Eq. 3) [-]		0.3295	
c_3 *	kirchner parameter 3 (see Eq. 3) [-]		-0.07757	
ae_scale_factor *	scaling factor for actual evapotranspiration [-]		1.43	
tx *	temperature threshold rain/snow [°C]		-0.92	
wind_const *	determining wind profile [-]		6.32	
wind_scale *	determining wind profile [-]		1.12	
snowfall_reset_depth	minimum snowfall required to reset SSA [mm SWE]		5.0	
snow_cv_forest	snow CV in forested area [-]		0.17	
snow_cv_intercept	intercept of linear elevation-CV relation		-0.050	
snow_cv_slope	slope of linear elevation-CV relation		0.00056	
max_water	fractional max water content of snow [-]		0.10	
SSA _{snow}	SSA of fresh snowfall [m ² kg ⁻¹]		73.0	
surface_magnitude	Max snow depth for snow heat content [mm SWE]		33.0	
max_surface_layer **	Maximum thickness of surface layer [mm SWE]	16.0	8.0	4.0
depo_factor **	Multiplication factor for deposition [-]	0.5	1.0	1.5
scav_phob **	scavenging ration of hydrophobic BC [-]	0.03	0.3	0.003
scav_phil **	scavenging ration of hydrophilic BC [-]	2.0	0.2	0.02

Table 3. Average change in discharge during the early (March 22 to May 29) and late (May 30 to August 10) melt season of min, mid, and max scenario and average change in SWE during the melt season (March 22 to August 10) compared to the no-ARF scenario (zero BC mass deposition).

scenario	early melt season discharge		late melt season discharge		melt season SWE	
	[m ³ s ⁻¹]	[%]	[m ³ s ⁻¹]	[%]	[mm]	[%]
min estimate	0.2	2.5	-0.18	-0.8	-1.5	-2.1
mid estimate	0.81	9.9	-0.74	-3.1	-5.1	-7.4
max estimate	1.74	21.4	-1.60	-6.7	-10.3	-15.1

Table 4. Season mean volume error in discharge during the early (March 22 to May 29) and late (May 30 to August 10) melt season of no-ARF, min, mid, and max scenario compared to observed discharge. The percentage change shows an increase (+) or decrease(-) of the volume error compared to the no-ARF volume error.

scenario	early melt season discharge		late melt season discharge	
	[m ³ s ⁻¹]	[%]	[m ³ s ⁻¹]	[%]
no-ARF	-2.32	-	1.78	-
min estimate	-2.12	-8.7	1.60	-10.1
mid estimate	-1.52	-34.7	1.04	-41.6
max estimate	-0.57	-75.1	0.18	-89.8